Article

A chiral superlattice route to spin-split topological antiferromagnetism

https://doi.org/10.1038/s41586-026-11073-7

Received: 19 November 2025

Accepted: 24 August 2026

Published online: 7 October 2026

Check for updates

Thao Dinh[1,2,24], Mengke Liu[2,3,24]✉, Jian-Xiang Qiu[1]✉, Sougata Mardanya[4], Suk Hyun Sung[5,6], Xuan Hoang Le[1,2], Christopher Broyles[7], Chengfeng Zhu[1], Qiaozhi Xu[7], Haotian Chen[7], Zack Rehfuss[7], Yu-Fei Liu[1,2], Xiaoyu Zeng[1], Houchen Li[1], Peng Guo[1], Jinchen Liu[1], Tianye Huang[1], Jingtian Shi[8], Michael Smith[8], Joanna M. Blawat[9], John Singleton[9], Ross McDonald[9], Iván E. Arvizo[1], Dongtao Cui[1], Shao-Liang Zheng[1], Kenji Watanabe[10], Takashi Taniguchi[11], Vineet Kumar Sharma[4], Sudip Ghorai[12], Barun Ghosh[12], Hsin Lin[13], Ting Yong Lim[14], Tay-Rong Chang[14], Arun Bansil[15,16], Ivar Martin[8], Ashvin Vishwanath[2], Weiwei Xie[17], Claudia Felser[18], Jairo Sinova[19,20], Anyuan Gao[1], Mikhail D. Lukin[2], Jennifer E. Hoffman[2], Sugata Chowdhury[4], Qiong Ma[21], Kai Sun[22], Ismail El Baggari[5], Sheng Ran[7], Talieh S. Ghiasi[2,23], Hongkun Park[1,2], Philip Kim[2]✉ & Su-Yang Xu[1]✉

Chirality has emerged as a new mechanism for inducing spin and Berry-curvature phenomena in quantum materials and molecular chemistry[1–7]. Collinear antiferromagnets (AFMs) are promising for spintronics and topological magnetism, yet realizing large Berry curvature and spin-split bands remains challenging[8,9]. Here we report a chiral-superlattice route to spin-split topological phenomena from collinear antiferromagnetism. We study the collinear AFM UOTe, in which we show a spontaneous chiral superlattice arising from frozen chiral phonons at a finite wave vector. Without the superlattice, the pristine collinear AFM in UOTe has neither Berry curvature nor spin-split bands. When electrons move through the chiral superlattice, their orbital Bloch wavefunction and quantum geometry are modulated by the strong chiral superlattice potential, generating large Berry curvature, which we detect by the nonlinear Hall effect. At 150 K, the chiral-superlattice-induced Berry curvature couples to the collinear AFM order, leading to an anomalous Hall angle of about 0.14 abruptly near the Néel temperature T_N which is among the largest in bulk magnets. Moreover, our spin Hanle precession measurement shows that the chiral superlattice also generates spin-polarized current from the collinear AFM, a long-standing goal in spintronics. We shed light on the supermodulation formation mechanism based on chemical ion size and physical interlayer–intralayer energy competitions, which we use to propose a design principle to discover similar bond-mismatch superlattices, providing a chiral superlattice pathway through real-space engineering of quantum geometry[10,11].

The concept of superlattice has recently emerged at the forefront of quantum condensed matter physics, highlighted by the two-dimensional (2D) van der Waals (vdW) moiré heterostructures. Apart from the artificially constructed superlattices, some bulk materials can develop intrinsic long-range lattice modulations, forming natural superlattices. These naturally occurring superlattices offer potential advantages in structural uniformity and scalability[12]. Despite the recent interest[13–15], the mechanism of formation of natural superlattices is not well understood—most material discoveries are based on trial and error.

In this paper, we report the discovery of a natural chiral superlattice in the collinear antiferromagnet (AFM) UOTe. Collinear AFMs have long been regarded as promising platforms for spintronics, with the generation of large anomalous Hall effect (AHE) and spin-polarized current as central goals[8,9], motivating the recent explosion of alter-magnetism[16–23]. We show that the natural chiral superlattice offers a

[1]Department of Chemistry and Chemical Biology, Harvard University, Cambridge, MA, USA. [2]Department of Physics, Harvard University, Cambridge, MA, USA. [3]Department of Physics, University of Texas at Dallas, Richardson, TX, USA. [4]Department of Physics and Astronomy, Howard University, Washington, DC, USA. [5]The Rowland Institute at Harvard, Harvard University, Cambridge, MA, USA. [6]Michigan Center for Materials Characterization, University of Michigan, Ann Arbor, MI, USA. [7]Department of Physics, Washington University in St. Louis, St. Louis, MO, USA. [8]Materials Science Division, Argonne National Laboratory, Lemont, IL, USA. [9]National High Magnetic Field Laboratory, Los Alamos National Laboratory, Los Alamos, NM, USA. [10]Research Center for Electronic and Optical Materials, National Institute for Materials Science, Tsukuba, Japan. [11]Research Center for Materials Nanoarchitectonics, National Institute for Materials Science, Tsukuba, Japan. [12]S. N. Bose National Centre for Basic Sciences, Kolkata, India. [13]Institute of Physics, Academia Sinica, Taipei, Taiwan. [14]Department of Physics, National Cheng Kung University, Tainan, Taiwan. [15]Department of Physics, Northeastern University, Boston, MA, USA. [16]Quantum Materials and Sensing Institute, Northeastern University, Burlington, MA, USA. [17]Department of Chemistry, Michigan State University, Michigan, MI, USA. [18]Max Planck Institute for Chemical Physics of Solids, Dresden, Germany. [19]Institut für Physik, Johannes Gutenberg University, Mainz, Germany. [20]Department of Physics, Texas A&M University, College Station, TX, USA. [21]Department of Physics, Boston College, Chestnut Hill, MA, USA. [22]Department of Physics, University of Michigan Ann Arbor, Ann Arbor, MI, USA. [23]Kavli Institute of Nanoscience, Delft University of Technology, Delft, The Netherlands. [24]These authors contributed equally: Thao Dinh, Mengke Liu. ✉e-mail: mliu@utdallas.edu; jqiu@g.harvard.edu; philipkim@g.harvard.edu; suyangxu@fas.harvard.edu

new and effective way to functionalize collinear AFM for topological magnetic phenomena distinct from altermagnetism[16–23]. Moreover, we reveal the mechanism of formation of the chiral superlattice. Distinct from the moiré superlattice, the chiral superlattice in UOTe is a bond-mismatch superlattice, in which the superlattice strongly modifies the local covalent U–Te bond. This leads to a strong modulation whose energy scale is roughly one order of magnitude larger than typical moiré systems, enabling the real-space quantum geometry. Our work establishes a chiral superlattice route for realizing spin-split topological responses in collinear AFMs, extending the interplay between chirality and time-reversal-symmetry breaking[3–6] to topological magnetism, quantum geometry and natural superlattices.

Basic characterizations

UOTe is a recently synthesized vdW heavy-fermion-based magnet[24]. Structurally, UOTe has a layered, square crystal structure with the space group *P*4/*nmm* no. 129, shown in Fig. 1a. Magnetically, UOTe shows a collinear AFM order (Fig. 1a) with the Néel temperature $T_N \simeq 150$ K, reported by neutron scattering in ref. 24. Within the same vdW layer, the two U ions, labelled U1 and U2, are AFM-coupled with their spins along the $+z$ and $-z$ directions. The magnetic unit cell contains two vdW layers, with the spin configuration of $(+z, -z)$ $(-z, +z)$. This collinear AFM has $\mathcal{PT}$ and $t\mathcal{T}$ symmetries ($\mathcal{P}$, $\mathcal{T}$ and t are space-inversion, time-reversal and translation symmetries). Electronically, UOTe has a semimetallic ground state. Figure 1b shows the temperature-dependent resistance. The carrier density is as low as 2×10^{19} cm^{-3}.

Discovery of a chiral superlattice

We have performed transmission electron microscopy (TEM) measurements. Beyond the atomic structure, our TEM data show a long-range wavelike superlattice (Fig. 1c,d). The superlattice is found to be present up to 700 °C. The in-plane period of the superlattice is $a_s \approx 2.65\ \text{nm} \approx 6.7a$, therefore incommensurate with the atomic lattice. In reciprocal space, this corresponds to a finite wavevector $\mathbf{q} = \left(\frac{1}{6.7}\frac{2\pi}{a}, 0, \frac{1}{2}\frac{2\pi}{c}\right)$. Moreover, the superlattice in UOTe is unidirectional, which breaks the four-fold rotational symmetry of the atomic lattice (Supplementary Information section I.2).

We now visualize the atomic displacement pattern. Along the supermodulation axis $\hat{x}$, the displacement of U1—Fig. 1e (green arrows)—rotates within the (x, z) plane, from $-x$ to $+z$, then to $+x$, and finally to $-z$. Similarly, the displacement of U2 also rotates within the (x, z) plane but with the opposite chirality (additional TEM data are shown in Extended Data Fig. 1). These supermodulations of U1 and U2 can be viewed as the 'freezing' of chiral phonons[25] with opposite handedness (DFT phonon calculations in Fig. 1f and Extended Data Fig. 2).

We now show the existence of a net chirality in the superlattice. Our measured Δ_x^{U1} and Δ_x^{U2} have different shapes, as shown in Fig. 1i. The different shapes show that the opposite chiral displacements of U1 and U2 do not cancel. Such a net chirality breaks $\mathcal{PT}$ symmetry. Furthermore, $t\mathcal{T}$ symmetry is also broken because the in-plane supermodulation of adjacent layers has different lineshapes (Extended Data Fig. 1b). Moreover, the supermodulation leads to a monoclinic distortion, which breaks the C_{2x} symmetry (Extended Data Fig. 1a, inset). Overall, our TEM data show that the magnetic point group of UOTe is reduced to m_y' with the superlattice, confirmed by single-crystal X-ray diffraction measurements (Supplementary Information section I.3).

To further confirm the net chirality in the superlattice, we also performed optical circular dichroism[26,27]. At $T > T_N$, we expect only chiral circular dichroism. Our circular dichroism map at $T > T_N$ (Fig. 1j,k) identified chiral domains. The chiral superlattice reduces the symmetry to a ferromagnetic group. We detect the spontaneous net magnetization M_z by nitrogen-vacancy (NV) centre magnetometry. As shown in Fig. 1m, $M_z \approx 10\ \text{m}\mu_B$ per U ion—for comparison, the free moment of each U is about $3.2\ \mu_B$.

Spatially encoded Berry curvature

The chiral superlattice can modulate the low-energy Bloch wavefunction and quantum geometry in real space, generating strong Berry curvature. As the conduction electrons are composed of the U 6*d* orbitals, we describe the conduction electrons of UOTe by a two-component orbital wavefunction $|u_\mathbf{r}\rangle = \begin{pmatrix} C_{U1} \\ C_{U2} \end{pmatrix}$. This wavefunction is expressed on a Bloch sphere, in which the north and south poles correspond to the purely U1 and purely U2 6*d* states, and the equator corresponds to an equal-weight superposition. As the conduction electron moves through the superlattice, the Bloch wavefunction rotates strongly on the Bloch sphere between the U1 and U2 (Fig. 2a). Not only the Bloch wavefunction, but also the quantum geometry, such as Berry curvature, is spatially modulated. $x = 0$ is polarized to U2, which has left-handed $(z - ix)$ chiral displacement. This leads to opposite Berry curvature at $\pm k_y$, and therefore a finite Berry curvature dipole along k_y (calculations in Extended Data Fig. 3e). $x = a_s/2$ is polarized to U1, which has right-handed chiral displacement, which in turn leads to the opposite Berry curvature dipole. Owing to the net chirality, the opposite Berry curvature dipoles at $x = 0$ and $x = a_s/2$ do not cancel. Therefore, the final Berry curvature dipole of the chiral superlattice is nonzero, which can be detected by the nonlinear Hall effect.

We therefore perform nonlinear Hall (NLH) experiments. As shown in Fig. 2d, the nonlinear longitudinal signal, $V_{yyy}^{2\omega}$, is nearly zero, whereas the nonlinear Hall signal $V_{xyy}^{2\omega}$ shows a clear quadratic signal. We perform angular-dependent measurements. As shown in Fig. 2e, the nonlinear Hall signal is large for $V_{xyy}^{2\omega}$, but zero for $V_{yxx}^{2\omega}$, consistent with the large Berry curvature dipole along k_y. We further perform scaling analysis by temperature-dependent measurements. The scaling law (Fig. 2g) is linear, consistent with the Berry curvature dipole mechanism[28]. The nonlinear Hall conductivity is larger than that of the noncentrosymmetric Weyl semimetals WTe_2 (refs. 29,30) and $TaIrTe_4$ (ref. 31), suggesting the potential of the chiral supermodulation as a new and effective way for generating Berry curvature.

Chiral superlattice + AFM induces AHE

We have shown that the chiral superlattice generates strong Berry curvature through the spatial modulation of quantum geometry. The collinear AFM order can further strongly reshape the *k*-space distribution of the Berry curvature (Fig. 3a), leading to strong topological magnetic phenomena. Below T_N, we observe clear AHE that emerges abruptly near T_N (Fig. 3c), almost like a step function. The abrupt onset reflects the rapid lifting of *k*-space cancellation of opposite Berry curvature when AFM order sets in. We have addressed alternative possibilities, including weak ferromagnetism, critical scattering and sudden change of carrier mobility (Extended Data Fig. 4 and Supplementary Information sections VII.1 and VII.2). Large AHE persists at zero net magnetization and the intrinsic AFM contribution dominates (Extended Data Fig. 4). Moreover, to distinguish this from conventional Berry-curvature mechanisms, we performed additional measurements and calculations (Supplementary Information section VII.3). These measurements show that the chiral superlattice is important in generating Berry curvature by breaking the relevant symmetries. Once the symmetries are broken by the chiral superlattice, the strong spin–orbit coupling of the U–Te electronic structure is likely to be important for the large magnitude. Moreover, calculations in Supplementary Information section II.7 predict that pressure may suppress the superlattice, providing a possible route to test whether the Berry-curvature response is correspondingly reduced.

The AHE angle (about 0.14) is the largest in AFMs and one of the largest in bulk magnets[22,23,32–42]. We further perform scaling analysis based on temperature-dependent measurements (Fig. 3g).

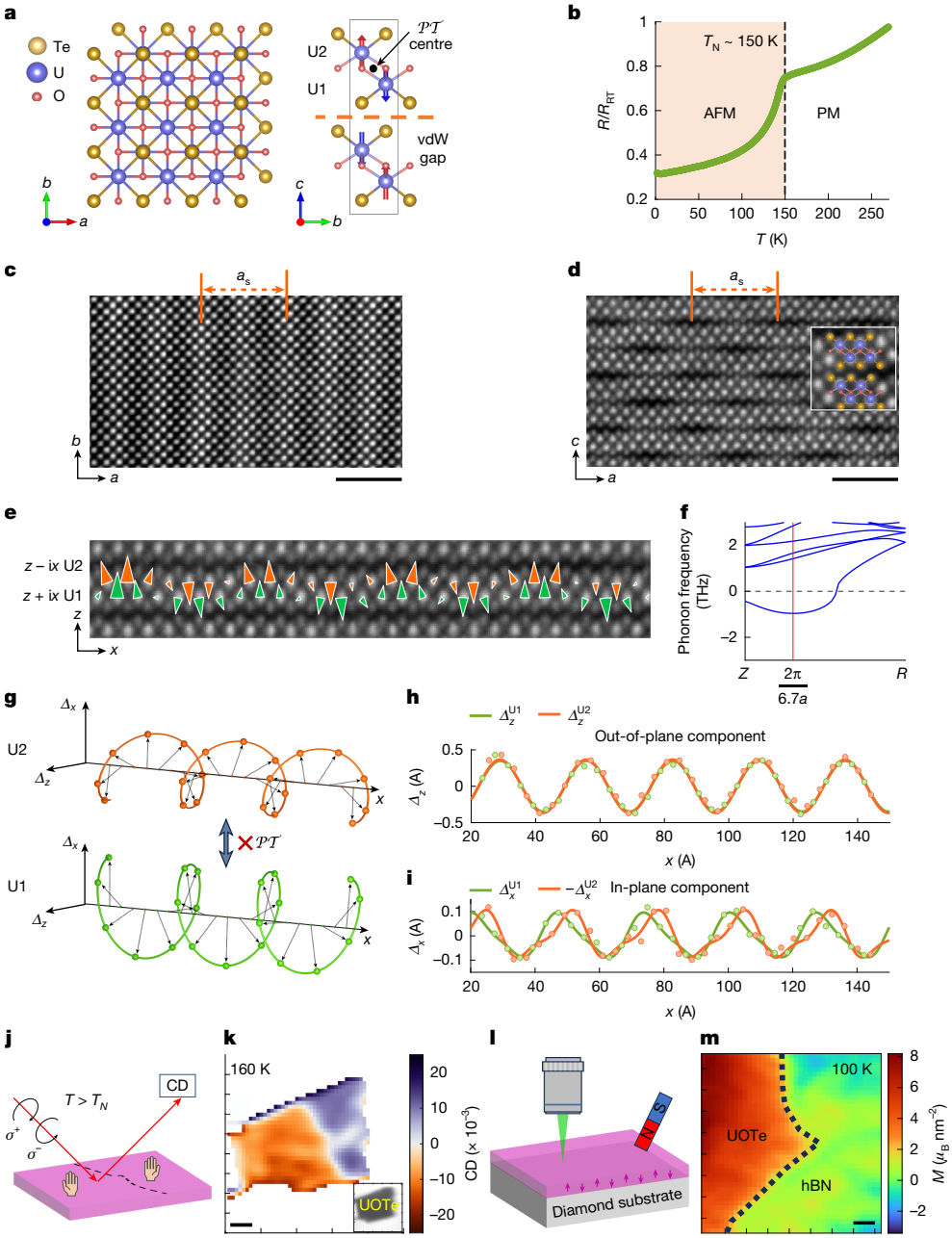


Fig. 1 | Discovery of a natural superlattice with 2D planar chirality in the collinear AFM UOTe. a, Crystal structure and collinear AFM of UOTe. **b**, Resistance of UOTe flake (13.3 nm) shows metallic temperature dependence. **c**,**d**, Plan-view and cross-sectional view of STEM of UOTe. A spontaneous superlattice with an in-plane period $a_s \approx 6.7a$ is observed. **e**, Cross-sectional STEM image of one UOTe vdW layer. The arrows represent the displacement of U1 and U2. **f**, Magnified view of the DFT-calculated phonon dispersion of UOTe. See full dispersion in Extended Data Fig. 2. The negative phonon frequency at finite wavevector **q** is consistent with the experimentally observed **q** for the superlattice. **g**, Schematic of the atomic displacements for U1 and U2, which have opposite chiral winding structures. The opposite winding structures have slightly different amplitudes and therefore do not cancel each other. This spontaneous chiral imbalance leads to a net chirality, which breaks $\mathcal{PT}$ symmetry. **h**,**i**, Measured out-of-plane and in-plane atomic displacements for U1 and U2. The in-plane displacements Δ_x^{U1} and Δ_x^{U2} have visibly different shapes, which confirm that the opposite chiral displacements of U1 and U2 do not cancel. Circles denote TEM data points, and lines denote fitting of the TEM data. The fitting parameter values are shown as layer 11 in Extended Data Table 1. **j**,**k**, Optical circular dichroism (CD) setup and data at $T = 160$ K. **l**,**m**, Diamond nitrogen-vacancy (NV) centre magnetometry setup and net magnetization map of a UOTe flake measured by NV magnetometry at 100 K. Scale bars, 2 nm (**c**,**d**); 5 μm (**k**); 1 μm (**m**).

Using $\sigma_{AHE} = \sigma_{AHE}^{intrinsic} + C^{skew}\sigma_{Drude}^2$, we obtain $\sigma_{AHE}^{Intrinsic} \simeq 160$ S cm^{-1} or 0.34 e^2/h per layer.

Spin-polarized current

Another crucial low-energy magnetic phenomenon is the spin-polarized current. Large spin-polarized current in collinear AFMs is highly desired[8,9,16–22] but remains very rare. UOTe is a promising candidate: the small chiral imbalance makes the net magnetization small, whereas the relevant U 5*f*-derived bands lie below the Fermi level and do not contribute to the Fermi surface (Supplementary Fig. 52). By contrast, the spin-polarized current arises from the Fermi surface states derived from the U 6*d* orbitals.

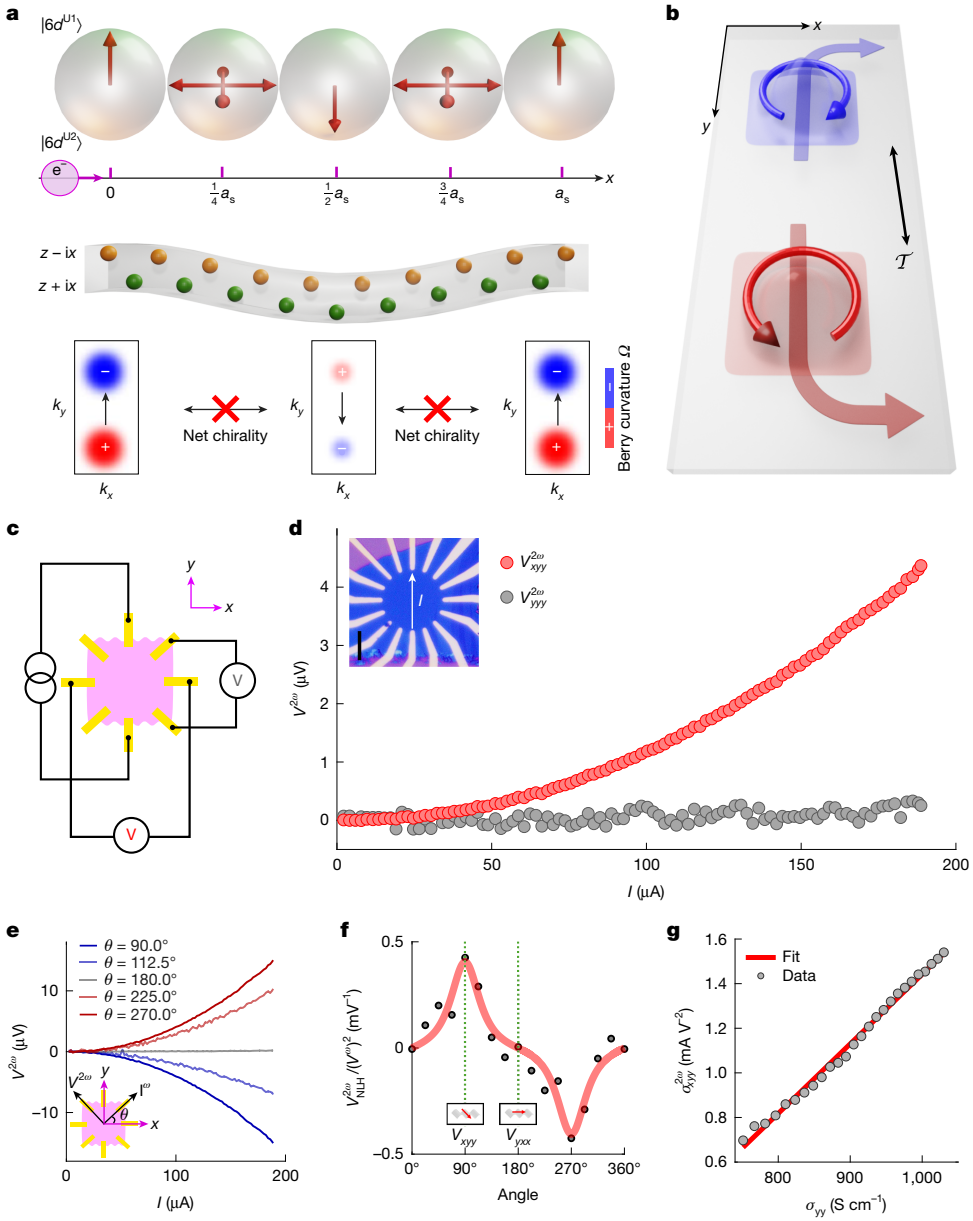


Fig. 2 | Chiral supermodulation generates strong Berry curvature. a, The conduction electrons composed of U 6*d* orbitals can be described by a two-component wavefunction. As the conduction electron moves through the superlattice, both the Bloch wavefunction and the Berry curvature dipole are spatially modulated (see text). **b**, The net Berry curvature dipole along k_y can be detected by a nonlinear Hall effect where the incident current is along *y*, and the resulting Hall voltage is along *x*. **c**, Schematic measurement setup. **d**, Nonlinear transport measurement of UOTe at $T = 250$ K. The inset shows the optical image of UOTe device. **e**,**f**, Angular-dependent nonlinear Hall measurements at $T = 250$ K. The directions of both the incident current I^{ω} and the nonlinear Hall voltage $V^{2\omega}$ are rotated simultaneously with respect to the crystalline directions. The angular-dependent measurements show a large nonlinear Hall signal when the incident current is along *y*, revealing the directional Berry curvature dipole along k_y. **g**, The nonlinear Hall conductivity as a function of the Drude conductivity obtained from temperature-dependent measurements between 200 K and 300 K. Scale bar, 10 μm (**d**, inset).

To directly measure the spin-polarized current generation by UOTe, we fabricated a standard graphene-based spin-transport Hanle device (Fig. 4a,b). Figure 4c shows the measured Hanle precession of the UOTe-injected spins in graphene. As expected, the detected nonlocal spin signal $R_{nl}(B)$ follows the Hanle profile: the signal is small near $B_x = 0$, then grows as B_x increases. Moreover, the Hanle signals change polarity and become nearly opposite (Fig. 4c, blue and red curves). Subtracting the two curves isolates the pure Hanle precession signal (Fig. 4d). These systematic observations provide evidence for the spin-polarized currents from the collinear AFM UOTe.

We fit our Hanle data to obtain the spin injection efficiency $\eta_{Injection}$—the spin polarization injected into graphene, which provides a lower bound of the Fermi surface spin polarization $S_z^{E_F}$ of UOTe (see details in the Methods, section 'Spin transport'). We obtain a spin injection efficiency of $\eta_{Injection} = 5.40 \pm 0.99\%$. Additional UOSe/graphene Hanle experiments as well as DFT calculations of the UOTe/graphene proximity effect are discussed in Supplementary Information section VIII.3. These systematic data, taken collectively, support the intrinsic spin-polarized current generated by the chiral superlattice. To further strengthen this conclusion, future Hanle experiments in which the chiral superlattice can be switched in situ on and off would be desirable.

Theoretical modelling

To confirm the chiral-superlattice-induced Berry curvature and the resulting topological magnetic phenomena, we have built a minimal

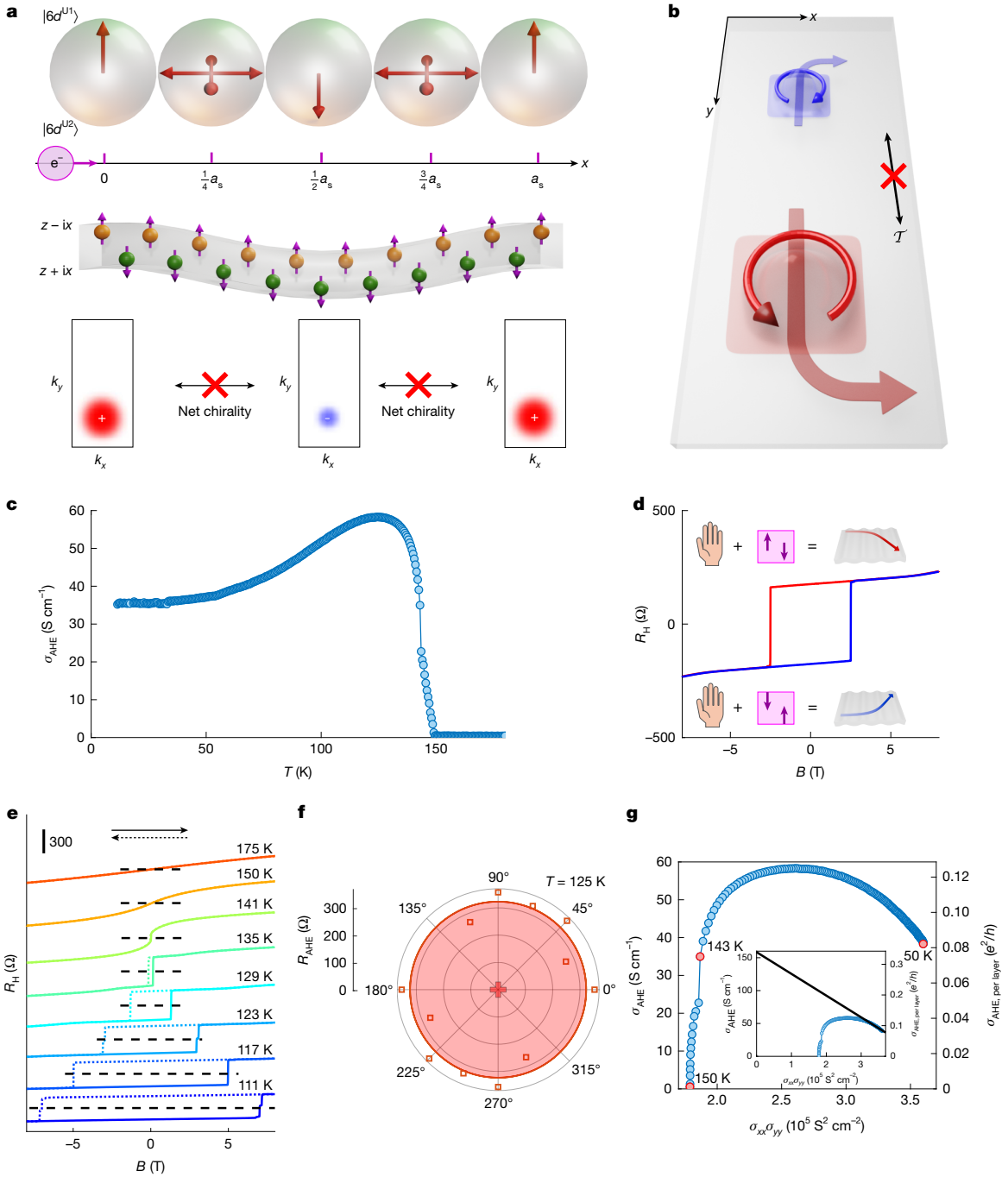


Fig. 3 | Chiral superlattice plus AFM generates large anomalous Hall angle. a, The collinear AFM order can break the cancellation between opposite Berry curvatures at $\pm k_y$: $x = 0$ and $x = a_s/2$ have opposite total Berry curvature, which do not cancel because of the net chirality. **b**, The net Berry curvature in k-space generates the AHE. **c**, Temperature dependence of AHE conductivity. **d**, Magnetic field dependence of the Hall resistivity at 125 K, showing a pronounced anomalous Hall hysteresis loop. **e**, Temperature evolution of the AHE, showing a coercive field reaching up to 8 T near 110 K. **f**, Angular dependence of the anomalous Hall resistance at 125 K. **g**, Scaling behaviour of AHE signal. The inset shows the fitting of $\sigma_{AHE} = \sigma_{AHE}^{intrinsic} + C^{skew}\sigma_{Drude}^2$ at 50 K < T < 100 K.

tight-binding model with the U 6*d* orbitals on a chiral potential modulation that is derived from the chiral superlattice TEM displacement pattern. The spatial modulation of the Berry curvature is directly seen from the model in Extended Data Fig. 3e. The resulting superlattice band structure has large Berry curvature with opposite sign at $\pm k_y$ (Extended Data Fig. 3b). We find notable Berry curvature dipole D_{yz} around 1–2 nm near the Fermi energy (Extended Data Fig. 3c), consistent with the value (approximately 1.62 nm) derived from our nonlinear Hall data (see Supplementary Information section IX.4.5). Further inclusion of the AFM order into the model lifts the cancellation between the contributions at $\pm k_y$, thus leading to a net Berry curvature (Extended Data Fig. 3f–j). The chiral supermodulated AFM band structure is a spin-split semimetal (Supplementary Fig. 49), facilitating large spin-polarized current (Fig. 4e,f and Supplementary Fig. 52). We also used DFT to calculate the chiral superlattice band structure for quantitative comparison with experiments. A reasonable agreement between data and calculation regarding the AHE conductivity and AHE angle is achieved (Supplementary Information sections 3.3, 3.4 and 4.4).

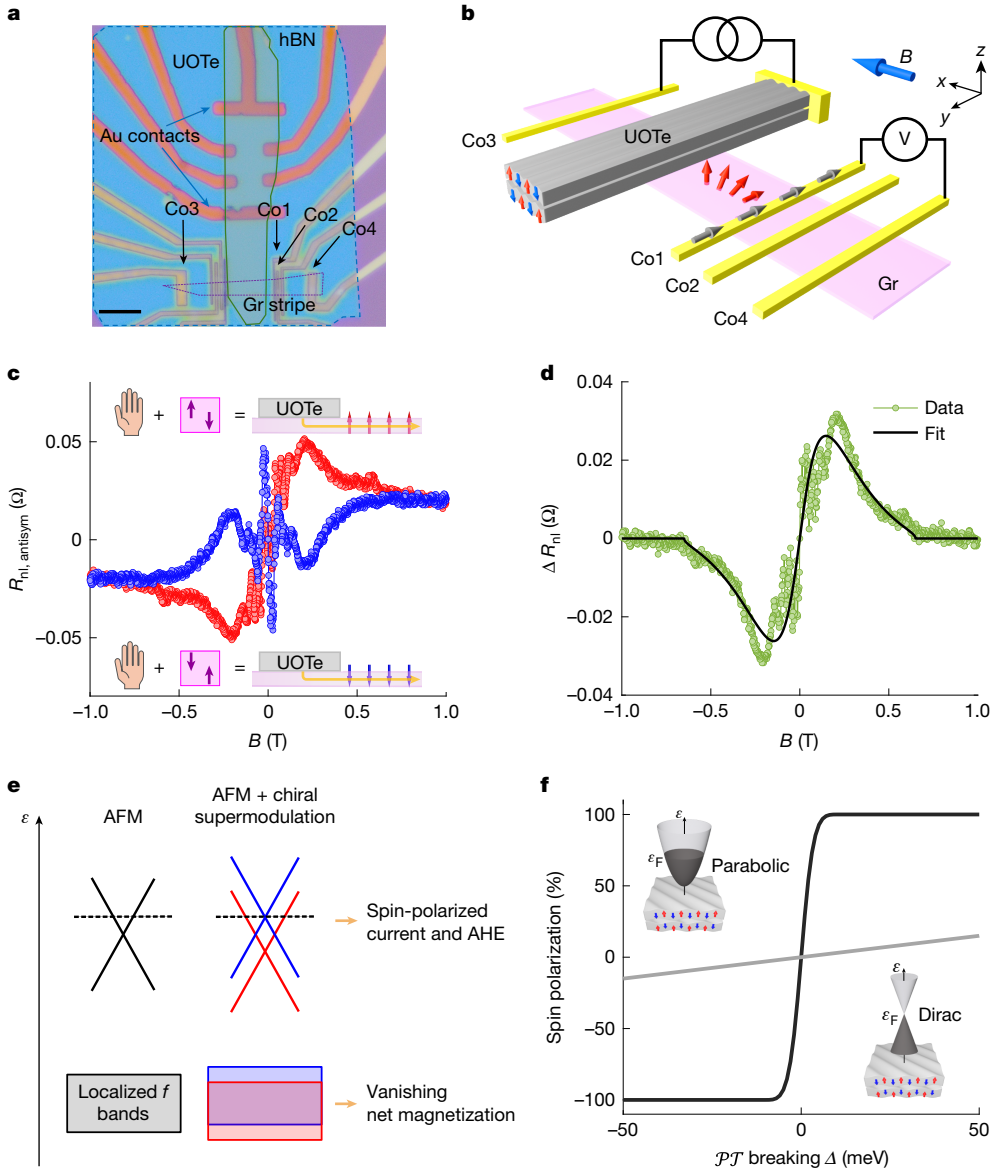


Fig. 4 | Spin-polarized current from the chiral supermodulated collinear antiferromagnetism. a,**b**, Schematic and optical image of a nonlocal spin-transport device consisting of a UOTe flake as the spin injector, Al_2O_3/Co contacts as the spin detectors, and a monolayer graphene channel for spin transport. The UOTe thickness is 27 nm. **c**, In-plane magnetic field dependence of the nonlocal resistance measured at 1.7 K after initializing UOTe in AFM I and AFM II states, while the Co detector magnetization was held fixed. **d**, Hanle signal curve fitted to the solution of the time-independent Bloch equations for a uniform spin diffusion system (see details in the main text). **e**, The small chiral imbalance means that the net magnetization will be small. Moreover, in UOTe, the relevant U 5*f*-derived bands lie below the Fermi level and do not contribute to the Fermi surface. The Fermi-level electrons are small pockets whose contribution to the net magnetization is naturally small. By contrast, the spin-polarized current is determined only by the spin polarization of the Fermi surface. UOTe features spin-split semimetal bands near the Fermi level. The spin polarization of the current is naturally large. **f**, Model-calculated spin polarization of the current as a function of the symmetry-breaking Δ. Scale bar, 10 μm (**a**).

Superlattice formation and design

Motivated by the strong topological magnetic phenomena observed in UOTe, we uncovered the formation mechanism of the chiral supermodulation. UOTe consists of two distinct covalent bonds, U–O and U–Te. The supermodulation originates from the mismatch between the distinct covalent bonds, which leads to competition between interlayer bonding (energy gain) and intralayer repulsion (energy cost) that drives the supermodulation instability. The mechanism can be visualized by comparing UOS and UOTe (Extended Data Fig. 5). UOS has an additional interlayer bond connecting the U with the S in the next layer, which is enabled by the large S–U–S angle (82°). This interlayer bond lowers energy. However, forming similar interlayer bonding in UOTe would laterally stretch the U–O–U central block because of the much longer U–Te bond length, which is more energetically costly. As a result, in the nominal unit cell of UOTe, the Te–U–Te bond angle is much smaller (77°), which hinders the interlayer bonding. To form interlayer bonding while keeping the central block unstretched, the layers locally curve up or down with opposite signs in adjacent layers (Extended Data Fig. 6), which is exactly the supermodulation. In this way, at specific locations, the Te–U–Te angle opens up (81°), enabling the interlayer U–Te covalent bonding. The cost is that, at some other locations, the Te–U–Te angle decreases (73°), leading to an intralayer repulsion. This mechanism naturally explains the existence of opposite chirality (Supplementary Information section II.3). The net chirality can be understood as a follow-up transition due to interlayer

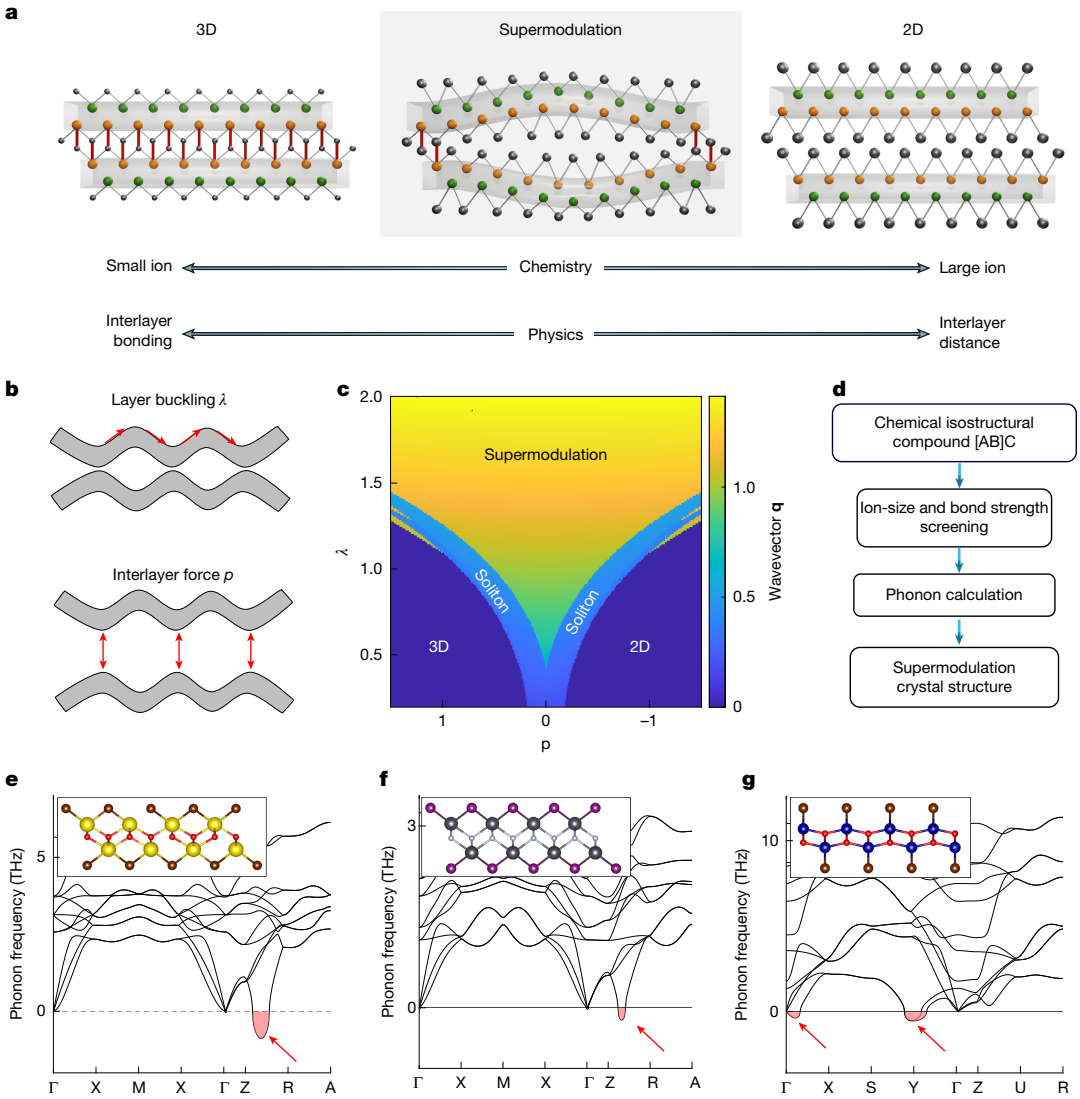


Fig. 5 | Formation mechanism and design principle for chiral supermodulations. a, The chiral supermodulation is an intermediate phase between the 3D covalent and 2D vdW phases because of the competition between the interlayer bonding and intralayer repulsion energies that can be tuned by chemical ion sizes. **b**, Illustration of the layer buckling λ and interlayer force p that appear in the free energy. **c**, Phase diagram as a function of λ and p, showing the supermodulation as an intermediate phase between 3D covalent and 2D vdW phases, with additional exotic soliton–superlattice phases at the boundaries between supermodulation and 2D/3D phases (see Supplementary Information section II.1). **d**, A flow chart for searching for similar chiral supermodulation in other materials. **e**–**g**, DFT-calculated phonon dispersions showing similar instability in other materials (PrOBr (**e**), PbFI (**f**), CrOBr (**g**)).

bonding anharmonicity (Supplementary Information section II.3). More broadly, this microscopic mechanism motivates a comparison between two types of superlattices, that is, the bond-mismatch superlattice such as UOTe and the lattice-mismatch superlattices such as moiré systems (Extended Data Fig. 7). Owing to the spatial modulation of covalent bonding, the modulation energy scale in UOTe is roughly one order of magnitude stronger (Supplementary Information section II.6), making the local quantum geometry a natural description of its physics. Hence, our data above show that the natural bond-mismatch superlattice can generate quantum geometrical physics, with a higher energy scale and a real-space picture. This provides a fresh perspective in designing superlattice materials.

The supermodulation can be understood as the intermediate phase between the 3D covalent lattice with interlayer bonding and 2D vdW lattice without interlayer bonding (Fig. 5a). A generic Ginzburg–Landau theory can be written as $F=-\alpha\psi^2+\beta\psi^4+p\psi+\lambda\psi\frac{\mathrm{d}^2\psi}{\mathrm{d}x^2}+\gamma\left(\frac{\mathrm{d}^2\psi}{\mathrm{d}x^2}\right)^2$, where $\psi(x)$ is the interlayer distance. The first two terms provide a standard double-well free-energy profile for the 2D vdW and 3D covalent phases, which can be switched by varying the interlayer force p. The crucial new term $\lambda\psi\frac{\mathrm{d}^2\psi}{\mathrm{d}x^2}$ provides an energy gain when the layer curves; the new term $\gamma\left(\frac{\mathrm{d}^2\psi}{\mathrm{d}x^2}\right)^2$ adds an energy penalty for finite curvature. The supermodulation shows up as an intervening phase (Fig. 5c). Moreover, our model predicts exotic soliton superlattices at the boundaries (Supplementary Information section II.1). This formation mechanism is verified by calculating the phonon dispersions of the UOX class (Extended Data Fig. 6c).

Based on the above mechanism and phenomenological theory, we propose a design principle that goes from chemistry to physics to materials (Fig. 5a,d and Extended Data Fig. 8). From chemistry, we can tune the size of the ions and the strength of chemical bonds. To physics, the above chemical tuning of ion size and bond strength effectively controls the interlayer bonding and intralayer repulsion energies. To materials, there are about 500 isostructural compounds (Extended Data Fig. 8c), generically written as ABC. We have

developed an empirical rule based on material parameters such as the ion size and the ratios of bond lengths (Extended Data Fig. 8 and Supplementary Information section II.4). For example, the ratio $r_1 = \frac{\text{Interlayer A} - \text{C bond length}}{\text{Intralayer A} - \text{C bond length}} > 1.1$ is an indicator for supermodulation. Based on this design principle, we have theoretically identified promising candidates (see Fig. 5e–g and Supplementary Information section II.5).

Outlook

Looking forward, it would be of interest to perform time-domain pump–probe experiments, in which the pump-induced oscillation of the frozen chiral phonons can lead to dynamical control of the observed topological magnetic phenomena. It would be further interesting to study the pressure effect to search for the new soliton–superlattice phase. More broadly, our work opens up a pathway to similar bond-mismatch superlattices with large modulation energy scales, including magnetic, superconducting and quantum-light-source materials, for new physics, chemistry and device concepts.

Online content

Any methods, additional references, Nature Portfolio reporting summaries, source data, extended data, supplementary information, acknowledgements, peer review information; details of author contributions and competing interests; and statements of data and code availability are available at https://doi.org/10.1038/s41586-026-11073-7.

1. Bloom, B. P., Paltiel, Y., Naaman, R. & Waldeck, D. H. Chiral induced spin selectivity. *Chem. Rev.* **124**, 1950–1991 (2024).
2. Chang, G. et al. Topological quantum properties of chiral crystals. *Nat. Mater.* **17**, 978–985 (2018).
3. Yu, F. H. et al. Concurrence of anomalous Hall effect and charge density wave in a superconducting topological kagome metal. *Phys. Rev. B* **104**, L041103 (2021).
4. Guo, C. et al. Switchable chiral transport in charge-ordered kagome metal CsV_3Sb_5. *Nature* **611**, 461–466 (2022).
5. Guo, C. et al. Distinct switching of chiral transport in the kagome metals KV_3Sb_5 and CsV_3Sb_5. *npj Quantum Mater.* **9**, 20 (2024).
6. Elmers, H. J. et al. Chirality in the kagome metal CsV_3Sb_5. *Phys. Rev. Lett.* **134**, 096401 (2025).
7. Luo, J. et al. Large effective magnetic fields from chiral phonons in rare-earth halides. *Science* **382**, 698–702 (2023).
8. Jungwirth, T., Marti, X., Wadley, P. & Wunderlich, J. Antiferromagnetic spintronics. *Nat. Nanotechnol.* **11**, 231–241 (2016).
9. Šmejkal, L., Mokrousov, Y., Yan, B. & MacDonald, A. H. Topological antiferromagnetic spintronics. *Nat. Phys.* **14**, 242–251 (2018).
10. Dong, L. & Niu, Q. Geometrodynamics of electrons in a crystal under position and time-dependent deformation. *Phys. Rev. B* **98**, 115162 (2018).
11. Yao, D., Go, D., Mokrousov, Y. & Murakami, S. Dynamical orbital angular momentum induced by circularly polarized phonons. *Phys. Rev. Lett.* **137**, 066301 (2026).
12. Gao, Y., Lee, P., Coppens, P., Subramania, M. A. & Sleight, A. W. The incommensurate modulation of the 2212 Bi-Sr-Ca-Cu-O superconductor. *Science* **241**, 954–956 (1988).
13. Devarakonda, A. et al. Clean 2D superconductivity in a bulk van der Waals superlattice. *Science* **370**, 231–236 (2020).
14. Qian, Q. et al. Chiral molecular intercalation superlattices. *Nature* **606**, 902–908 (2022).
15. Devarakonda, A. et al. Evidence of striped electronic phases in a structurally modulated superlattice. *Nature* **631**, 526–530 (2024).
16. Jungwirth, T. et al. Symmetry, microscopy and spectroscopy signatures of altermagnetism. *Nature* **649**, 837–847 (2026).
17. Chen, H., Niu, Q. & MacDonald, A. H. Anomalous Hall effect arising from noncollinear antiferromagnetism. *Phys. Rev. Lett.* **112**, 017205 (2014).
18. Šmejkal, L., Sinova, J. & Jungwirth, T. Beyond conventional ferromagnetism and antiferromagnetism: a phase with nonrelativistic spin and crystal rotation symmetry. *Phys. Rev. X* **12**, 031042 (2022).
19. Mazin, I.The PRX Editors Editorial: altermagnetism—a new punch line of fundamental magnetism. *Phys. Rev. X* **12**, 040002 (2022).
20. Cheong, S.-W. & Huang, F.-T. Altermagnetism classification. *npj Quantum Mater.* **10**, 38 (2025).
21. Song, C. et al. Altermagnets as a new class of functional materials. *Nat. Rev. Mater.* **10**, 473–485 (2025).
22. Nakatsuji, S., Kiyohara, N. & Higo, T. Large anomalous Hall effect in a non-collinear antiferromagnet at room temperature. *Nature* **527**, 212–215 (2015).
23. Nayak, A. K. et al. Large anomalous Hall effect driven by a nonvanishing Berry curvature in the noncolinear antiferromagnet Mn_3Ge. *Sci. Adv.* **2**, e1501870 (2016).
24. Broyles, C. et al. UOTe: Kondo-interacting topological antiferromagnet in a van der Waals lattice. *Adv. Mater.* **37**, 2414966 (2025).
25. Juraschek, D. M. et al. Chiral phonons. *Nat. Phys.* **21**, 1532–1540 (2025).
26. Papakostas, A. et al. Optical manifestations of planar chirality. *Phys. Rev. Lett.* **90**, 107404 (2003).
27. Bai, B., Svirko, Y., Turunen, J. & Vallius, T. Optical activity in planar chiral metamaterials: theoretical study. *Phys. Rev. A* **76**, 023811 (2007).
28. Sodemann, I. & Fu, L. Quantum nonlinear Hall effect induced by Berry curvature dipole in time-reversal invariant materials. *Phys. Rev. Lett.* **115**, 216806 (2015).
29. Ma, Q. et al. Observation of the nonlinear Hall effect under time-reversal-symmetric conditions. *Nature* **565**, 337–342 (2019).
30. Kang, K., Li, T., Sohn, E., Shan, J. & Mak, K. F. Nonlinear anomalous Hall effect in few-layer WTe_2. *Nat. Mater.* **18**, 324–328 (2019).
31. Kumar, D. et al. Room-temperature nonlinear Hall effect and wireless radiofrequency rectification in Weyl semimetal $TaIrTe_4$. *Nat. Nanotechnol.* **16**, 421–425 (2021).
32. Ye, L. et al. Massive Dirac fermions in a ferromagnetic Kagome metal. *Nature* **555**, 638–642 (2018).
33. Li, P. et al. Giant room temperature anomalous Hall effect and tunable topology in a ferromagnetic topological semimetal Co_2MnAl. *Nat. Commun.* **11**, 3476 (2020).
34. Sakai, A. et al. Giant anomalous Nernst effect and quantum-critical scaling in a ferromagnetic semimetal. *Nat. Phys.* **14**, 1119–1124 (2018).
35. Kim, K. et al. Large anomalous Hall current induced by topological nodal lines in a ferromagnetic van der Waals semimetal. *Nat. Mater.* **17**, 794–799 (2018).
36. Liu, E. et al. Giant anomalous Hall effect in a ferromagnetic kagome-lattice semimetal. *Nat. Phys.* **14**, 1125–1131 (2018).
37. Liu, Z. Q. et al. Electrical switching of the topological anomalous Hall effect in a non-collinear antiferromagnet above room temperature. *Nat. Electron.* **1**, 172–177 (2018).
38. Ghimire, N. J. et al. Large anomalous Hall effect in the chiral-lattice antiferromagnet $CoNb_3S_6$. *Nat. Commun.* **9**, 3280 (2018).
39. Feng, Z. et al. An anomalous Hall effect in altermagnetic ruthenium dioxide. *Nat. Electron.* **5**, 735–743 (2022).
40. Gonzalez Betancourt, R. D. et al. Spontaneous anomalous Hall effect arising from an unconventional compensated magnetic phase in a semiconductor. *Phys. Rev. Lett.* **130**, 036702 (2023).
41. Reichlova, H. et al. Observation of a spontaneous anomalous Hall response in the Mn_5Si_3 *d*-wave altermagnet candidate. *Nat. Commun.* **15**, 4961 (2024).
42. Yamada, R. et al. A metallic *p*-wave magnet with commensurate spin helix. *Nature* **646**, 837–842 (2025).

Publisher's note Springer Nature remains neutral with regard to jurisdictional claims in published maps and institutional affiliations.

Springer Nature or its licensor (e.g. a society or other partner) holds exclusive rights to this article under a publishing agreement with the author(s) or other rightsholder(s); author self-archiving of the accepted manuscript version of this article is solely governed by the terms of such publishing agreement and applicable law.

© The Author(s), under exclusive licence to Springer Nature Limited 2026

Methods

Bulk crystal growth

The growth of UOTe was performed in a two-zone furnace, using equimolar ratios of depleted uranium (sourced from New Brunswick Laboratory) and tellurium (99.9999%, sourced from Alfa Aesar). Growth details are in ref. 24. The source materials were sealed in an evacuated quartz tube, together with 1 mg cm^{-3} iodine. The ampoule was placed in a two-zone furnace, gradually heated up and held in the temperature gradient of 1,030/970 °C for 7 days, after which it was cooled to room temperature. The crystal structure was determined by X-ray powder diffraction using a Rigaku X-ray diffractometer with Cu-Kα radiation.

UOTe device fabrication

All fabrication steps involving UOTe were carried out in an argon-filled glovebox without exposure to air, heat or solvents. For the charge transport devices, thin flakes of UOTe were mechanically exfoliated from bulk crystals onto SiO_2/Si substrates. Electrical contacts (Cr/Au, 5 nm/35 nm) were deposited by e-beam evaporation through a pre-patterned SiN stencil mask. A protective hexagonal boron nitride (BN) layer (20–50 nm thick) was then transferred onto the UOTe flake. For the spin-transport devices, monolayer graphene flakes were mechanically exfoliated onto SiO_2/Si wafers and identified by optical microscopy. Spin detector contacts (Al_2O_3/Co/Au) were defined using standard e-beam lithography and deposited by e-beam evaporation. Thin UOTe flakes were exfoliated onto a PDMS stamp and subsequently transferred onto the graphene channel. Hall bar contacts (Cr/Au, 5 nm/35 nm) were deposited on UOTe using the same stencil mask method described above. A BN flake was transferred onto the final heterostructure to encapsulate and protect both UOTe and the Co contacts from air exposure. For both device types, wire bonding was performed inside the glovebox. The bonded chip carrier was sealed under argon by applying vacuum grease along the rim of the chip carrier and covering it with a glass slide. For the nitrogen-vacancy centre magnetometry measurements, thin UOTe flakes were exfoliated onto a PDMS stamp and transferred onto the diamond substrate.

TEM measurements and data analysis

Annular dark-field scanning transmission electron microscopy (STEM) was performed on a Thermo Fisher Scientific (TFS) Themis Z G3, operated at 200 keV with a convergence semi-angle of 18.9 mrad. Twenty rapid acquisition frames were registered and averaged to produce drift-free, high signal-to-noise ratio images. Supermodulation manifests as satellite peaks in Fourier space. Therefore, an image of pristine, undistorted lattice without periodic lattice displacements can be obtained by damping relevant Fourier components[43]. By comparing atomic coordinates of the original image and the Fourier-damped image, we extract the supermodulation displacement. The atomic coordinates were extracted using the Atomap package[44] (see also Supplementary Information section I.1). The precise superlattice in-plane period is determined by diffraction in TEM to be 6.686 ± 0.001. Cryogenic ADF-STEM was performed on a TFS Spectra 300 operated at 300 keV with a convergence semi-angle of 21.4 mrad, with a Mel-build double-tilt LN2 Vacuum Transfer Holder. The lineshapes of different layers in Extended Data Fig. 1b suggest (pseudo-)periodicity, which is also reflected in the fitted ϕ_q compared with a layer in Extended Data Fig. 1c. By contrast, the diffraction data (Supplementary Fig. 2) do not show a corresponding satellite peak in the q_z direction, excluding long-range ordering. Possible short-range order requires further investigation, but tT is broken regardless because the pseudo-periodicity does not correspond to an odd number of layers.

We further fit the TEM displacement data using the following expression:

$$\Delta_{U1} = A_z^{U1}\cos(qx)\hat{z} + A_x^{U1}\sin(qx+\phi_q^{U1})\hat{x} + B_x^{U1}\sin(2qx+\phi_{2q}^{U1}),$$
$$\Delta_{U2} = A_z^{U2}\cos(qx)\hat{z} - A_x^{U2}\sin(qx+\phi_q^{U2})\hat{x} + B_x^{U2}\sin(2qx+\phi_{2q}^{U2}).$$

The fitted values are shown in Extended Data Fig. 1 and the Extended Data Tables 1 and 2.

Based on the above displacements, we can mathematically derive an order parameter Ψ that breaks both inversion symmetry and mirror symmetry—the net chirality (see Supplementary Information section IX.1 for derivation)

$$\Psi^3 = -(A_x^{U1})^2 B_x^{U2}\cos(\phi_{2q}^{U2} - 2\phi_q^{U1}) + (A_x^{U2})^2 B_x^{U1}\cos(\phi_{2q}^{U1} - 2\phi_q^{U2}). \quad (1)$$

From the expression of the order parameter above, we can see that the system has no net chirality, when and only when $A_x^{U1} = A_x^{U2}, B_x^{U1} = B_x^{U2}$, $\phi_q^{U1} = -\phi_q^{U2}$ and $\phi_{2q}^{U1} = -\phi_{2q}^{U2}$. No net chirality corresponds to $\Psi = 0$. The system has net chirality when the above conditions are not satisfied. The above condition shows that our TEM data show net chirality. Our 300 K data (Extended Data Fig. 1) show that ϕ_{2q}^{U1} and ϕ_{2q}^{U2} have the same sign. Our 100 K data (Extended Data Fig. 1) show that not only do the U1 and U2 phases have the same sign, but also the amplitudes A_x^{U1} and A_x^{U2} show observable differences. In Supplementary Fig. 6, we provide simulations and intuition for the different terms (amplitudes and phases for first and second harmonics) and how they lead to net chirality. We can see that in case 1, if we only turn on the first harmonic z and x modulations with opposite phases, the $x + iz$ (orange) and $x - iz$ (green) modulations are perfectly symmetric with respect to the inversion centre. In case 2, if we add second-harmonic x modulation with opposite phases, the $x + iz$ (orange) and $x - iz$ (green) modulations are perfectly symmetric with respect to the inversion centre. In case 3, if we change the second-harmonic modulation of U1 and U2 to have the same phase, the $x + iz$ (orange) and $x - iz$ (green) modulations are not symmetric any more.

Optical measurements

Linear dichroism. The superlattice breaks the C_{4z} symmetry, enabling a nonzero optical linear dichroism. This linear dichroism signal can be used to distinguish the orthogonal superlattice domains, $\mathbf{q} \| a$ and $\mathbf{q} \| b$.

Circular dichroism. Circular dichroism can arise from both chirality and net magnetization. The circular dichroism measurements were performed in reflection mode with oblique incidence to avoid the cancellation of the chirality-induced circular dichroism signal (the optical activity) at normal incidence due to time-reversal symmetry[45–47]. At $T > T_N$, circular dichroism only arises from chirality; the corresponding optical activity tensor is σ_{xyy}, which is nonzero in the group m_y'. At $T < T_N$, an additional contribution from magnetization arises. However, we can use the magnetic field hysteresis measurements to separate them (Supplementary Information section III.3). The magnetic circular dichroism is antisymmetric with the magnetic field (the hysteresis loop part), whereas the chiral circular dichroism is symmetric with respect to the magnetic field (a nonzero offset).

Experimental methods. Optical linear and circular dichroism measurements were performed in the magneto-optical cryostat OptiCool by Quantum Design using a supercontinuum laser SuperK Extreme by NKT photonics. A spectrometer SpectraPro-300i by Acton Research was used to select the wavelength. The beam went through a photoelastic modulator. The retardation was half-wave for linear dichroism and quarter-wave for circular dichroism. Oblique incidence was achieved by sending the laser beam through one side of the objective. The oblique angle was about 10° at most. The reflected beam went through the top window of the cryostat, was collimated by the same objective and collected by an avalanche photodiode.

Nitrogen-vacancy centre magnetometry measurement

We used a (100)-oriented electronic-grade CVD-grown diamond (Element Six), mechanically thinned down to 50 μm and polished. A shallow ensemble of nitrogen-vacancy centres was created by ^{14}N ion implantation. Nitrogen-vacancy centre magnetometry, as reported in previous work[48], was performed based on the standard optically detected magnetic resonance. We used a 532-nm solid-state green laser, around 1 mW modulated by an acousto-optic modulator. The control microwave pulses are generated by IQ mixing, using a microwave generator and analogue control pulses produced by a high-sampling-rate arbitrary waveform generator (AWG). The signal was amplified by a medium-gain (Mini-Circuits ZX60-6013E-S+) and a high-gain, high-power amplifier (Mini-Circuits ZHL-25W-63+). Timing of all optical pulses, AWG trigger and data acquisition was orchestrated by a high-speed programmable pulse generator (SpinCore PulseBlasterESR-PRO-USB-RM2). A flake of UOTe and a flake of Fe_3GeTe_2 were both transferred onto the same diamond chip. We performed nitrogen-vacancy centre magnetometry on both flakes (see data in Supplementary Information section IV).

Charge transport

Linear charge anisotropy and AHE. Consider a crystal with both anisotropy and AHE. The linear resistivity can be written as

$$\begin{pmatrix} \rho_{xx} & \rho_{xy} \\ \rho_{yx} & \rho_{yy} \end{pmatrix} = \begin{pmatrix} \rho_{aa}\cos^2(\theta)+\rho_{bb}\sin^2(\theta) & (\rho_{aa}-\rho_{bb})\cos(\theta)\sin(\theta)-\rho_{\mathrm{AHE}} \\ (\rho_{aa}-\rho_{bb})\cos(\theta)\sin(\theta)+\rho_{\mathrm{AHE}} & \rho_{aa}\sin^2(\theta)+\rho_{bb}\cos^2(\theta) \end{pmatrix},$$

where a, b are the principal crystalline directions, x, y are the lab coordinates and x is the direction of the applied bias, and θ is the angle between a and x. Based on this resistivity tensor, we explain how we measured the charge anisotropy and AHE in UOTe. The longitudinal resistance ρ_{ii} can measure the charge anisotropy, that is, $\rho_{aa} \neq \rho_{bb}$ (Supplementary Information section VI.1.1). The transverse resistance $\rho_{yx} = \rho_{yx}^{\mathrm{aniso.}} + \rho_{\mathrm{AHE}}$ contains both anisotropy and AHE contributions. $\rho_{yx}^{\mathrm{aniso.}} = (\rho_{aa}-\rho_{bb})\cos(\theta)\sin(\theta)$ has a d-wave angular pattern and is symmetric with B field (Supplementary Information section VI.1.2). ρ_{AHE} is angular-independent and is antisymmetric with B field (Fig. 3d,e).

The conductivity tensor was then obtained by inverting the resistivity tensor $\begin{pmatrix} \sigma_{xx} & \sigma_{xy} \\ \sigma_{yx} & \sigma_{yy} \end{pmatrix} = \frac{1}{\rho_{xx}\rho_{yy}-\rho_{xy}\rho_{yx}} \begin{pmatrix} \rho_{yy} & -\rho_{yx} \\ -\rho_{xy} & \rho_{xx} \end{pmatrix}$. The AHE conductivity was then obtained by antisymmetrizing the off-diagonal conductivity $\sigma_{\mathrm{AHE}} = \frac{\sigma_{yx}-\sigma_{xy}}{2}$.

Nonlinear Hall conductivity. The nonlinear Hall conductivity can be obtained from the injected current I^{ω} along y, the measured nonlinear Hall voltage $V_{xyy}^{2\omega}$, as well as the linear resistances, by $\sigma_{xyy}^{2\omega} = \frac{V_{xyy}^{2\omega}}{I_y^{\omega 2} R_{yy}^2 R_{xx}} \frac{l^3}{w^2 d}$.

Experimental methods. Transport measurements were performed in a Quantum Design Dynacool PPMS system with a base temperature of 1.7 K and a maximum magnetic field of 9 T. For electrical transport measurements, longitudinal and transverse voltages were recorded simultaneously using standard low-frequency lock-in techniques (SR830 lock-in amplifiers), with the magnetic field applied along the out-of-plane direction.

Spin transport

We fabricated a spin-transport device using a standard nonlocal geometry and performed Hanle spin precession measurements in both the UOTe–Co configuration (Fig. 4) and Co–Co configuration (Supplementary Information section VIII.2.1). The same monolayer graphene serves as the spin-transport channel, whereas either a UOTe or Co contact is used as the spin injector and another Co contact as the spin detector.

To extract the spin polarization of spin injector and detector, we fit the UOTe–Co and the Co–Co Hanle signal curves to the corresponding solutions of the time-independent Bloch equations for a uniform spin diffusion system (Supplementary Information section VIII.2). Specifically, we make the following assumptions: (1) multiple Co contacts have the same spin polarization; and (2) in the UOTe–Co experiment, we consider only the spin injection at one edge of UOTe flake (closest to the Co detector contact). In this case, we neglect the spin diffusion and relaxation underneath UOTe. This also contributes to the fact that the extracted values provide a lower bound for the spin polarization of the UOTe-covered region. Under these assumptions, we fit the Co–Co Hanle curve to

$$R_{\mathrm{nl}} = (\eta_{\mathrm{Injection}}) \times \left(\frac{R_{\mathrm{sq}}\lambda_{\mathrm{spin}}\cos\varphi_1\cos\varphi_2}{2W_1} \frac{e^{-\frac{L_1}{\lambda_{\mathrm{spin}}}\sqrt{1-i\gamma_e B\tau}} + e^{-\frac{L_1}{\lambda_{\mathrm{spin}}}\sqrt{1+i\gamma_e B\tau}}}{\sqrt{1-i\gamma_e B\tau}+\sqrt{1+i\gamma_e B\tau}} \right) \times (\eta_{\mathrm{Detection}}).$$

The three brackets represent the three key parts of the Hanle experiment. $\eta_{\mathrm{Injection}}$ and $\eta_{\mathrm{Detection}}$, which both range from 0% to 100%, are the spin injection and detection efficiencies. Because both the injector and detector are Co electrodes prepared using the same recipe, we assume that $\eta_{\mathrm{Injection}} = \eta_{\mathrm{Detection}} = \eta_{\mathrm{Co}}$. The middle bracket characterizes spin propagation and precession, where γ_e is the electron gyromagnetic ratio, $R_{\mathrm{sq}} = 3.8\ \mathrm{k\Omega}$ is the graphene sheet resistance, $L_1 = 0.80\ \mu\mathrm{m}$ and $W_1 = 4.70\ \mu\mathrm{m}$ are the channel length and width, respectively, λ_{spin} is the spin relaxation length, τ is the spin lifetime, and $\varphi_{1,2}$ are the angles between the Co contact magnetization and its easy axis. By fitting the data in Supplementary Information section VIII.2.1, we get $\lambda_{\mathrm{spin}} = 2.17 \pm 0.46\ \mu\mathrm{m}$, $\tau = 235.66 \pm 83.04$ ps and $\eta_{\mathrm{Co}} = 1.03 \pm 0.11\%$.

We can proceed to fit the UOTe–Co Hanle curve by

$$R_{\mathrm{nl}} = (\eta_{\mathrm{Injection}}) \times \left(\frac{R_{\mathrm{sq}}\lambda_{\mathrm{spin}}\cos\varphi_1}{2W_2} \frac{e^{-\frac{L_2}{\lambda_{\mathrm{spin}}}\sqrt{1-i\gamma_e B\tau}} - e^{-\frac{L_2}{\lambda_{\mathrm{spin}}}\sqrt{1+i\gamma_e B\tau}}}{i(\sqrt{1-i\gamma_e B\tau}+\sqrt{1+i\gamma_e B\tau})} \right) \times (\eta_{\mathrm{Detection}}),$$

where $\eta_{\mathrm{Injection}}$ is the injection efficiency from UOTe, $\eta_{\mathrm{Detection}}$ is the detection efficiency by Co, which has been determined above, $R_{\mathrm{sq}} = 3.8\ \mathrm{k\Omega}$ is the graphene sheet resistance, $L_2 = 1.58\ \mu\mathrm{m}$ and $W_2 = 4.53\ \mu\mathrm{m}$ are the channel length and width. Note that the two equations are different because of the different injected spin direction (UOTe injects S_z, whereas Co injects S_y). By fitting the data in Fig. 4d, we get $\lambda_{\mathrm{spin}} = 1.02 \pm 0.15\ \mu\mathrm{m}$, $\tau = 49.76 \pm 14.68$ ps, and $\eta_{\mathrm{UOTe}} = 5.40 \pm 0.99\%$.

Tight-binding modelling

In this model, a unit cell contains two U sites, each of which has a $6d$ orbital, compatible with space group 129. Therefore, our minimal model has two bands. The Hamiltonian reads $H = -\sum_{\langle i,j\rangle} t_0(a_i^{\dagger}b_j + b_j^{\dagger}a_i)$. The chiral superlattice is then introduced as a slowly varying chiral potential modulation, derived from the chiral displacement pattern. The superlattice Hamiltonian reads $H_{\mathrm{s}} = -\sum_{\langle i,j\rangle} t(x)(a_i^{\dagger}b_j + b_j^{\dagger}a_i) + \sum_i V_1(x)a_i^{\dagger}a_i + \sum_j V_2(x)b_j^{\dagger}b_j$. If there is no chiral imbalance, then the U1 $z+ix$ and U2 $z-ix$ are related by the inversion symmetry and C_2 screw axis, therefore giving rise to a Dirac nodal crossing. The chiral imbalance then breaks the degeneracy between U1 $z+ix$ and U2 $z-ix$, opening up a gap at the nodal crossings. The resulting superlattice band structure has strong Berry curvature with opposite sign at $\pm k_y$ (Extended Data Fig. 3b), which is generated by the spatial modulation mechanism explained above. The spatial modulation of the Berry curvature $\Omega(x)$ is calculated by treating the slowly varying superlattice modulation as an adiabatic parameter and approximating each local region by a homogeneous tight-binding Hamiltonian $H(\mathbf{k}; x)$. The result is shown in Extended Data Fig. 3e, consistent with our intuitive picture in Fig. 2.

We can further include the AFM order. The supermodulated AFM Hamiltonian reads $H = H_s + H_{SOC} + H_{AFM}$, where $H_{AFM} = m\sum_i (a_{i\uparrow}^\dagger a_{i\uparrow} - a_{i\downarrow}^\dagger a_{i\downarrow}) - m\sum_j (b_{j\uparrow}^\dagger b_{j\uparrow} - b_{j\downarrow}^\dagger b_{j\downarrow})$ and $H_{SOC} = -\lambda_{SOC}\sum_{\langle i,j\rangle}(a_{i\uparrow}^\dagger a_{i\downarrow}^\dagger)(\hat{\mathbf{n}}_{ij}\cdot\sigma)\begin{pmatrix} b_{j\uparrow} \\ b_{j\downarrow}\end{pmatrix} + \text{h.c.}$

The AFM couples strongly to the Berry curvature through the spin–orbit coupling (SOC), lifting the cancellation between $\pm k_y$ and leading to a net Berry curvature in k-space, explaining the AHE. The chiral supermodulated AFM band structure is a spin Zeeman split semimetal. With such a low-energy band structure, the spin polarization of the current will be naturally large.

First-principles calculations

We used first-principles calculations within the DFT framework as implemented in the Vienna ab initio simulation package[49]. The electronic structure was calculated using the projector-augmented-wave pseudopotential, whereas the electron exchange-correlation effects were treated with the local density approximation. SOC was incorporated through j-dependent pseudopotentials. The energy cutoff of 450 eV was used for the plane-wave basis set, and the BZ integration was performed with a $5 \times 9 \times 5$ k-mesh. The total energy tolerance criterion was set to 10^{-6} eV. The onsite Coulomb potential was $U = 4$ eV so that the energy of the U 5f band matches the ARPES data (that is, $\simeq$2 eV below the Fermi level)[24]. For the atomic lattice, we used the experimentally determined lattice parameter in ref. 24. For the superlattice lattice structure, we used the TEM-fitted displacement (see expressions in section 'TEM measurements and data analysis'), changing only the periodicity to 7a (commensurate). Therefore, the level of chiral imbalance should serve as a reasonable reflection of the actually measured chiral imbalance by TEM. The DFT calculation yields the magnetic group m_y', which agrees with our TEM and X-ray diffraction experimental results above.

43. Savitzky, B. H. et al. Bending and breaking of stripes in a charge ordered manganite. *Nat. Commun.* **8**, 1883 (2017).
44. Nord, M., Vullum, P. E., MacLaren, I., Tybell, T. & Holmestad, R. Atomap: a new software tool for the automated analysis of atomic resolution images using two-dimensional Gaussian fitting. *Adv. Struct. Chem. Imaging* **3**, 9 (2017).
45. Fried, A. D. Relationship of time-reversal symmetry breaking to optical Kerr rotation. *Phys. Rev. B* **90**, 121112 (2014).
46. Armitage, N. P. Constraints on Jones transmission matrices from time-reversal invariance and discrete spatial symmetries. *Phys. Rev. B* **90**, 035135 (2014).
47. Hosur, P., Kapitulnik, A., Kivelson, S. A., Orenstein, J. & Raghu, S. Kerr effect as evidence of gyrotropic order in the cuprates. *Phys. Rev. B* **91**, 039908 (2015).
48. Andersen, T. I. et al. Electron-phonon instability in graphene revealed by global and local noise probes. *Science* **364**, 154–157 (2019).
49. Kresse, G. & Furthmüller, J. Efficient iterative schemes for *ab initio* total-energy calculations using a plane-wave basis set. *Phys. Rev. B* **54**, 11169–11186 (1996).

Acknowledgements We thank S.-W. Cheong, A. Devarakonda, R. M. Fernandez, T. Kurumaji, I. Mazin, N. Nagaosa and L. Ye for the discussions.

Author contributions T.D. fabricated the devices. S.H.S. performed the TEM measurements with help from M.L., T.D. and I.E.B., inspired by early STM measurements of M.L. and J.E.H.; J.-X.Q. initiated the optical measurements and performed optical linear and circular dichroism experiments with help from T.D. and X.Z.; T.D. performed the charge transport measurements with help from C.Z., M.L., Y.-F.L. and A.G.; T.S.G. conceived and designed the spin-transport and Hanle experiments, and supervised the measurements performed by T.D.; X.H.L. performed the nitrogen-vacancy centre magnetometry measurements with the help from T.D., M.D.L., H.P.; J.M.B., J. Singleton and R.M. performed the high-field magnetization measurements at LANL with the help from T.D.; I.E.A. performed the MPMS measurements with help from T.D. and D.C.; S.-L.Z. performed the single-crystal X-ray diffraction measurements with help from T.D.; C.B., Q.X., Z.R., H.C., W.X. and S.R. grew the UOTe single crystals. K.W. and T.T. grew the bulk hBN single crystals. S.M. performed first-principles calculations with help from B.G., V.K.S., S.G., H. Lin, T.-R.C., T.Y.L., A.B. and S.C.; K.S. performed effective modelling with help from J. Sinova and A.V.; M.S., J. Shi and I.M. proposed the free-energy model for the chiral superlattice. H. Li, P.G., J.L., T.H., C.F. and Q.M. helped with the charge transport experiments. T.D., M.L., J.-X.Q., P.K. and S.-Y.X. wrote the manuscript with contributions from others. S.-Y.X., P.K., and M.L. conceived the experiments. S.-Y.X. and P.K. supervised the project.

Funding T.D., J.-X.Q., M.S., J.M.B., R.M., Q.M., J. Shi, I.M., A.V. and S.-Y.X. were supported through the Center for the Advancement of Topological Semimetals (CATS), an Energy Frontier Research Center (EFRC) funded by the US Department of Energy (DOE) Office of Science, through the Ames National Laboratory under contract DE-AC0207CH11358. The work in SYX group was supported by the Office of Naval Research (ONR) grant no. N000142512285 (charge and spin transport), the National Science Foundation (NSF) career grant no. DMR-2143177 (fabrication), CATS (data analysis) and the Army Research Office (ARO) under W911NF2420195 Cooperative Agreement no. W911NF-24-2-0195 (manuscript writing). S.-Y.X. acknowledges the Alfred P. Sloan Foundation, the Camille and Henry Dreyfus Foundation, and Corning Fund for Faculty Development. P.K. acknowledges support from AFOSR grant no. FA9550-25-1-0019. T.D. acknowledges a partial support from AFOSR MURI grant no. FA9550-25-1-0262 (fabrication in the Kim group). Q.M. acknowledges support from the National Science Foundation (NSF) under award no. DMREF-2522383. H.P. and M.D.L. were supported by the GBMF grant no. 7797-01 and NSF CUA (PHY-1125846 for H.P. and M.D.L.). H.P., M.D.L., P.K. and S.-Y.X. are supported by the Samsung Electronics award no. A61703. TSG was supported by the Dutch Research Council (NWO) through a Rubicon grant (no. 019.222EN.013) and a Veni grant (no. VI.Veni.242.281). M.L. acknowledges the Harvard Quantum Initiative Postdoctoral Fellowship and the start-up funds at University of Texas at Dallas. J.E.H. was supported by the EPiQS Initiative of the Gordon and Betty Moore Foundation (GBMF) through grant GBMF10215. I.E.B. and S.H.S. acknowledge support by the Rowland Institute at Harvard. Research at Washington University was supported by the US DOE, Office of Science, Basic Energy Sciences grant no. DE-SC0026267 (sample synthesis) and the National Science Foundation (NSF) Division of Materials Research Award DMR-2236528 (high magnetic field measurement). Electron microscopy experiments were performed at the Michigan Center for Materials Characterization ((MC)^2, RRID: SCR_026770) and MIT.nano. Focused ion beam samples were prepared at (MC)^2 as well as at the Harvard University Center for Nanoscale Systems (CNS), a member of the National Nanotechnology Coordinated Infrastructure Network (NNCI), which is supported by the National Science Foundation under NSF award no. ECCS-2025158. A portion of this work was performed at the National High Magnetic Field Laboratory, which is supported by the National Science Foundation Cooperative Agreement no. DMR-2128556, the US DOE and the State of Florida. K.W. and T.T. were supported by the JSPS KAKENHI (21H05233 and 23H02052), the CREST (JPMJCR24A5), JST and World Premier International Research Center Initiative (WPI), MEXT, Japan. C.F. was supported by Deutsche Forschungsgemeinschaft through SFB 1143 (project ID 24731007) and the Würzburg-Dresden Cluster of Excellence ctd.qmat—Complexity, Topology and Dynamics in Quantum Matter (EXC 2147, project ID 390858490). H. Lin was supported by the National Science and Technology Council (NSTC) in Taiwan under grant no. NSTC 114-2112-M-001-055-MY3. T.R.C. was supported by the National Science and Technology Council (NSTC) in Taiwan (NSTC 114-2628-M-006-005-MY3 and NSTC113-2124-M-006-009-MY3), the National Cheng Kung University (NCKU), Taiwan, and the National Center for Theoretical Sciences, Taiwan. This research was supported, in part, by the Higher Education Sprout Project, Ministry of Education to the Headquarters of University Advancement at NCKU. T.-R.C. thanks the National Center for High performance Computing (NCHC) of the National Applied Research Laboratories in Taiwan for computational and storage resources. The work at the S. N. Bose National Centre for Basic Sciences (SNBNCBS) was supported by the Prime Minister Early Career Research Grant (PM-ECRG) from the Anusandhan National Research Foundation (ANRF), file number ANRF/ECRG/2024/003677/PMS, and also benefited from the PARAM-Rudra computational facility at SNBNCBS. The work at Northeastern University was supported by the National Science Foundation through the Expand-QISE award NSF-OMA-2329067 and benefited from the resources of the Advanced Scientific Computation Center of the Northeastern University, the Explorer Cluster, the Massachusetts Technology Collaborative award MTC-22032 and the Quantum Materials and Sensing Institute (QMSI). J. Sinova was supported by the US DOE, Office of Science, under award no. DE-SC0026038. We acknowledge the support to the X-ray core facility from the Major Research Instrumentation Program of the NSF under award no. 2216066. K.S. was supported by the GBMF10694.

Competing interests The authors declare no competing interests.

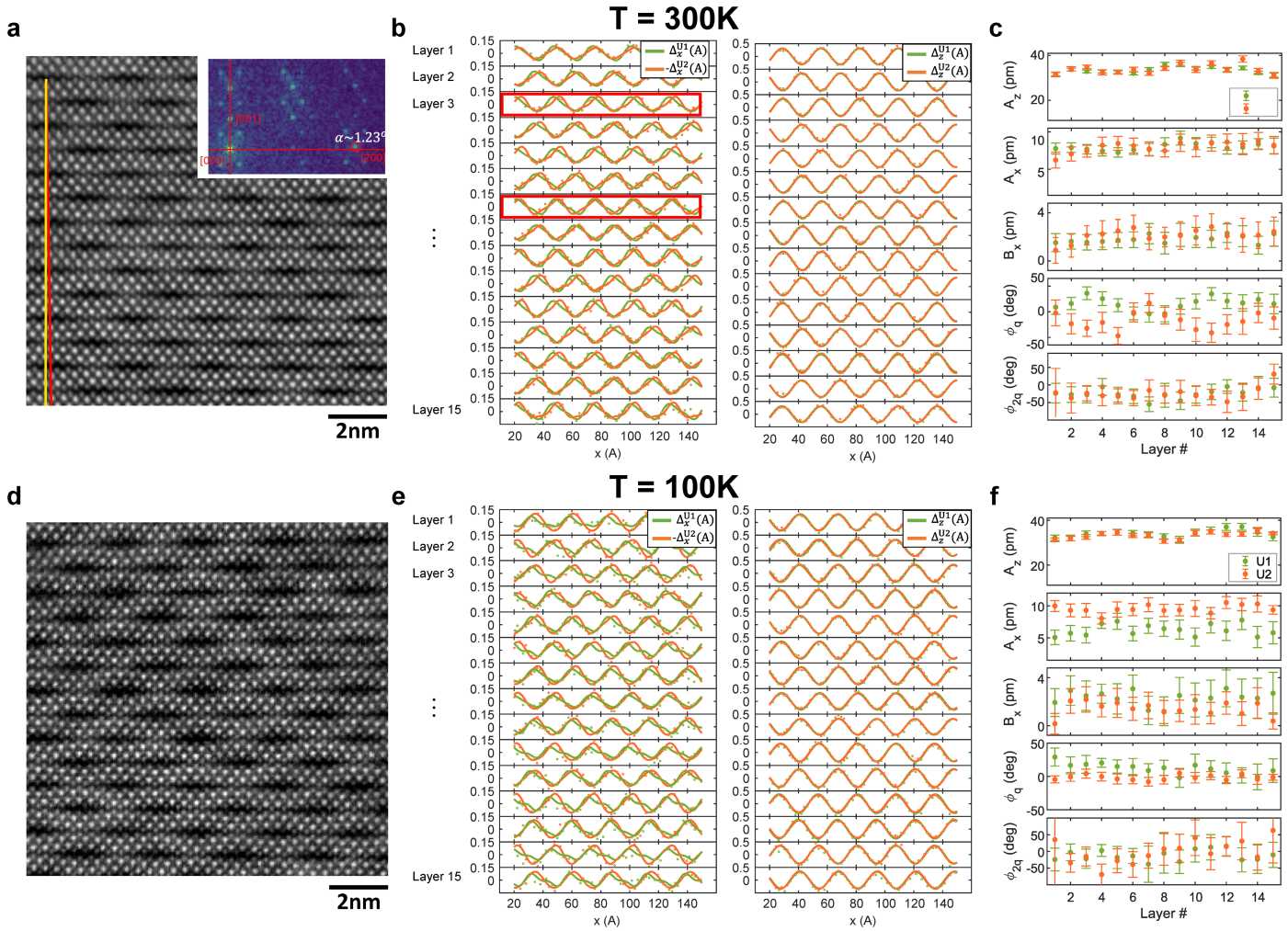
Additional information

Supplementary information The online version contains supplementary material available at https://doi.org/10.1038/s41586-026-11073-7.

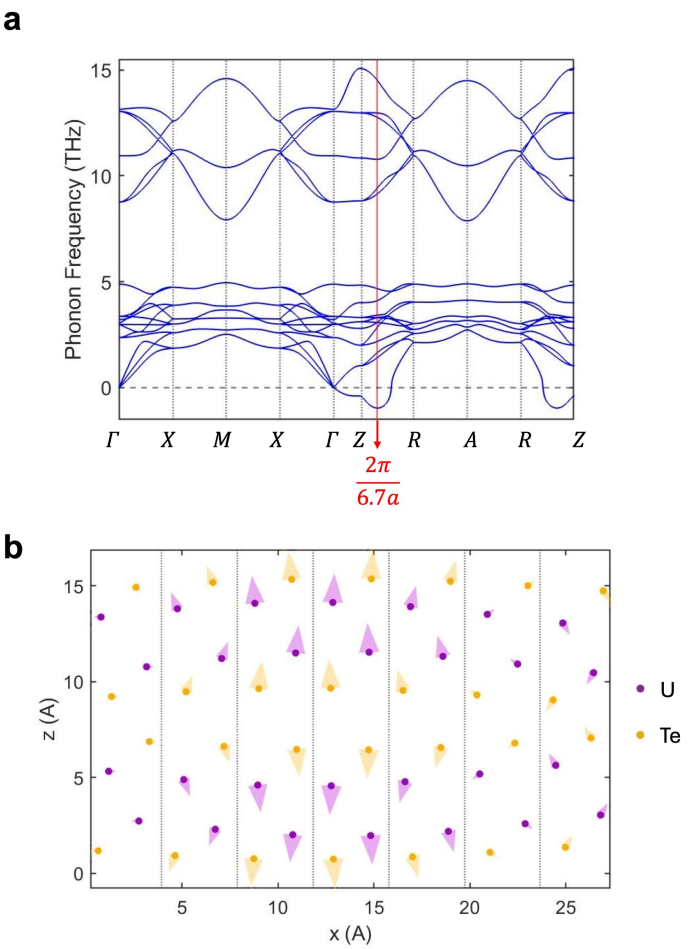
Correspondence and requests for materials should be addressed to Mengke Liu, Jian-Xiang Qiu, Philip Kim or Su-Yang Xu.

Peer review information *Nature* thanks Wei Jiang and the other, anonymous, reviewer(s) for their contribution to the peer review of this work. Peer reviewer reports are available.

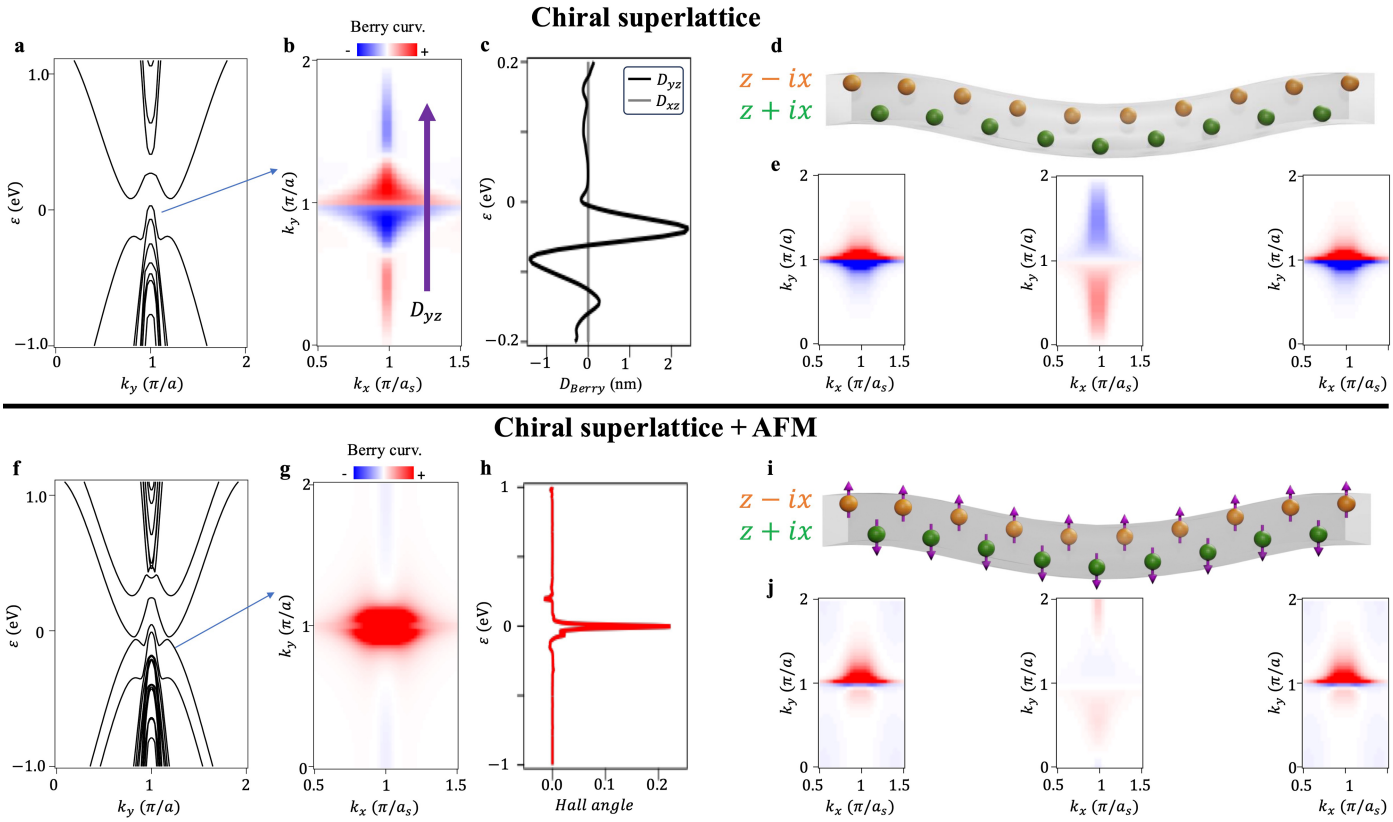
Reprints and permissions information is available at http://www.nature.com/reprints.



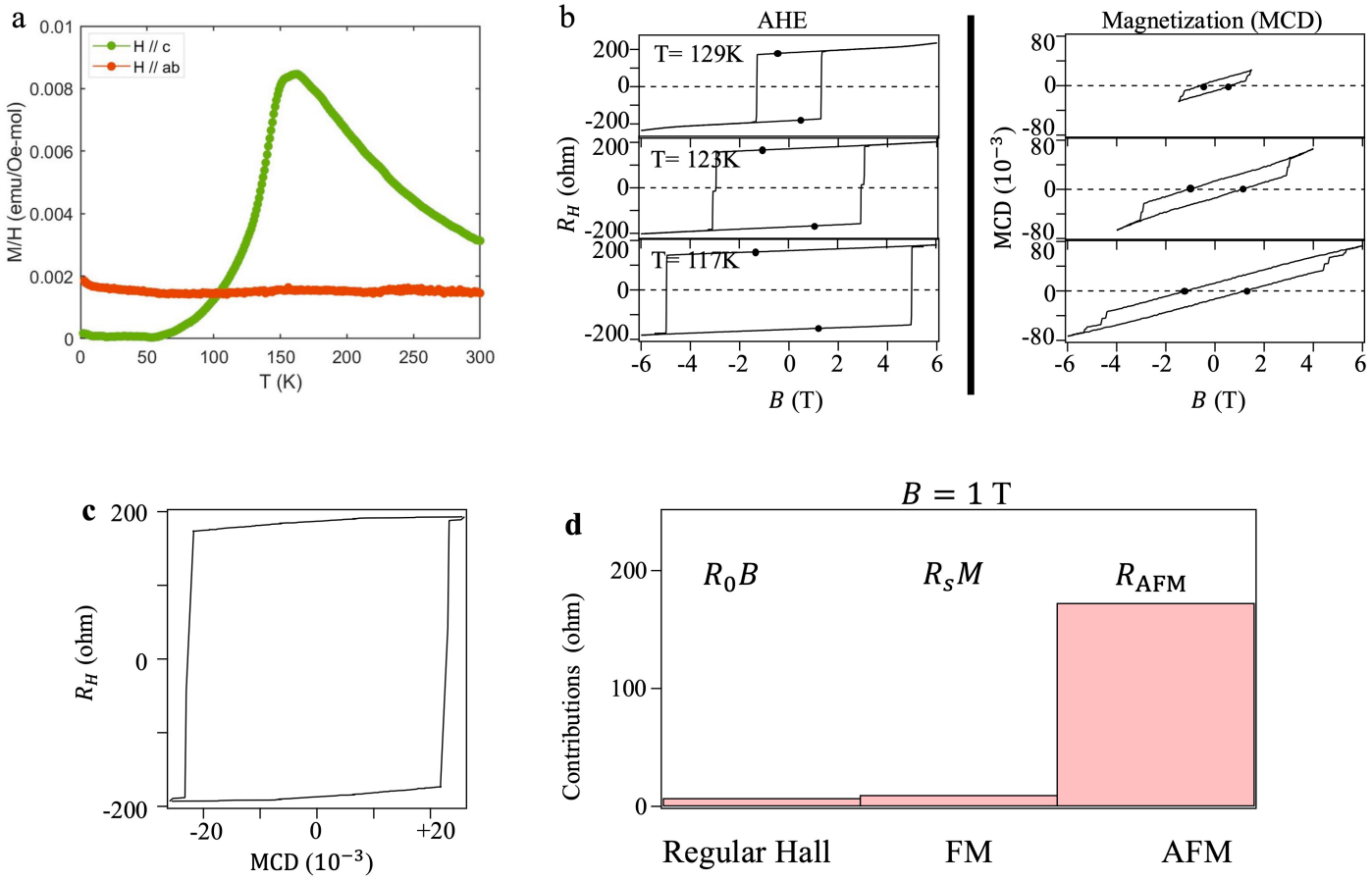
Extended Data Fig. 1 | Additional TEM at 300 K and 100 K in UOTe. **a-c**, Additional TEM data at 300 K. **a**, Cross-sectional STEM image of UOTe showing a monoclinic distortion. The red line connecting U atoms across layers deviates from the vertical yellow reference line, visualizing the cumulative shear associated with the monoclinic distortion. Inset: Electron diffraction pattern acquired from the same cross-sectional region, revealing a monoclinic distortion angle of $\alpha \sim 1.23°$. **b**, Fitted displacement parameters of U atoms across 15 UOTe layers. See Methods. 3 for the expressions for fitting the TEM data. The in-plane displacements of different layers have different lineshapes (for example, one can compare the highlighted red boxes). Therefore $t\mathcal{T}$ symmetry is also broken. **c**, Fitted values for each layer. **d-f**, Same as panels **a-c** but for TEM data at 100 K.



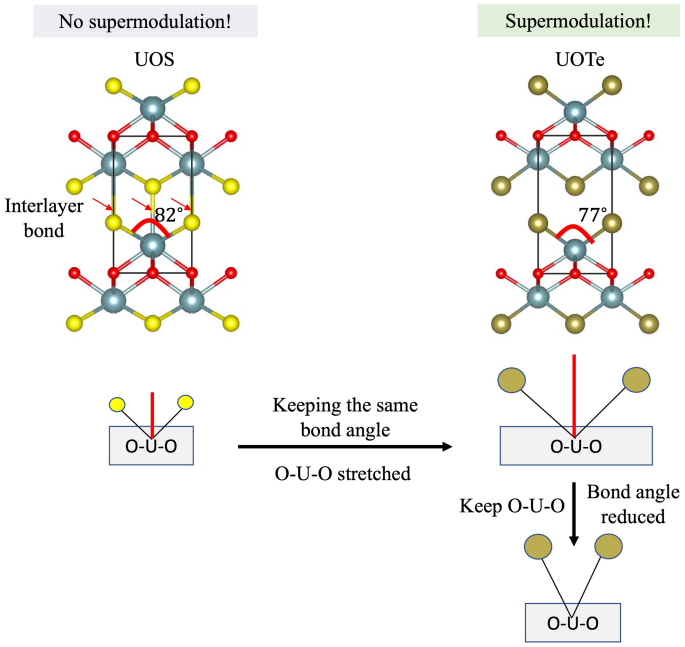
Extended Data Fig. 2 | DFT-calculated phonon band structure and displacement of UOTe without superlattice. a, DFT-calculated phonon band structure of UOTe. One branch of phonon has negative frequency at $\mathbf{q} = \left(\frac{1}{6.7}\frac{2\pi}{a}, 0, \frac{1}{2}\frac{2\pi}{c}\right)$, consistent with the experimentally observed **q** for the superlattice. **b**, Atomic displacements corresponding to that unstable phonon at the negative frequency. U1 and U2 (also Te1 and Te2) have opposite chiral winding structures, consistent with the experimental findings.



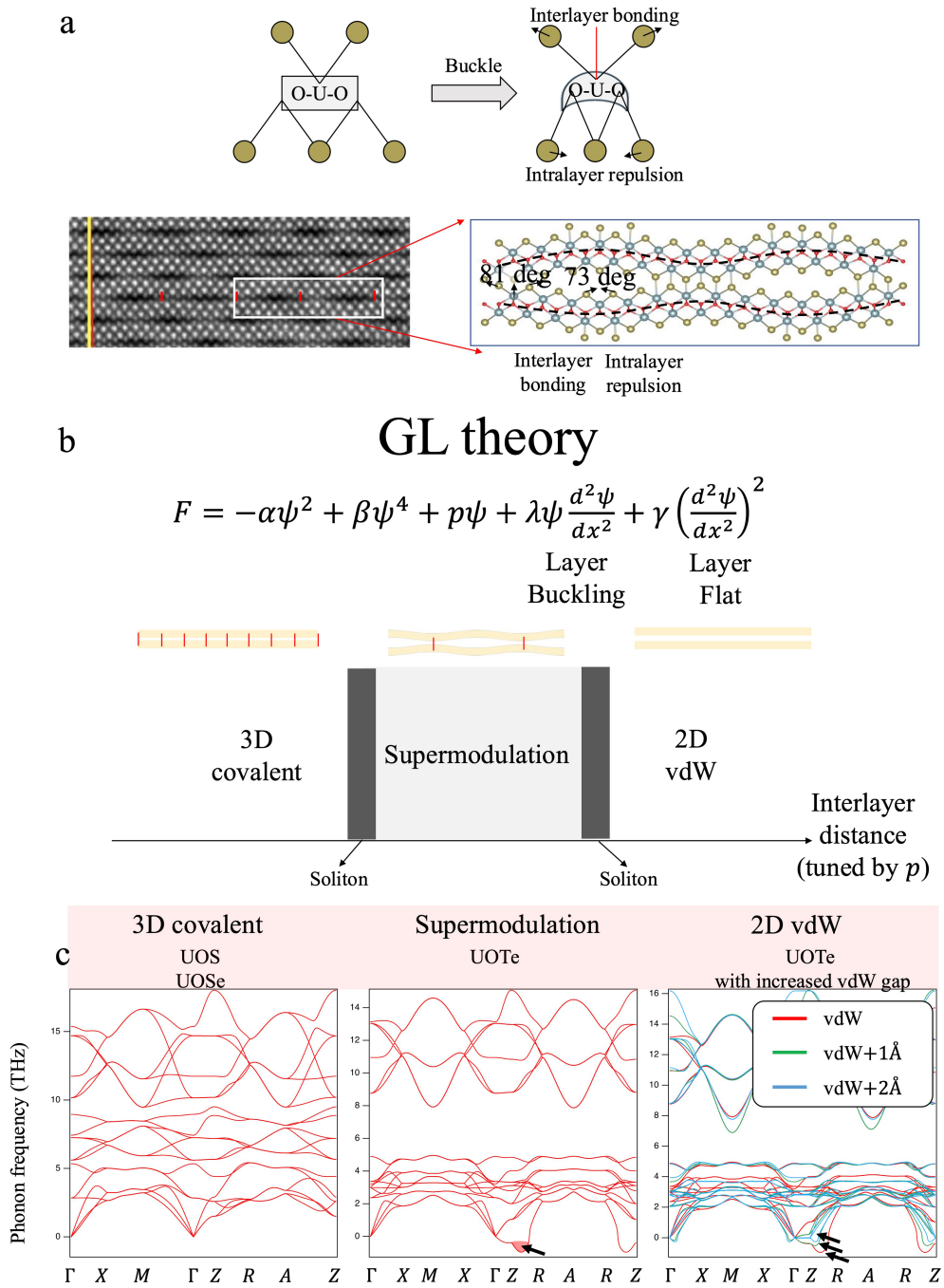
Extended Data Fig. 3 | Theoretical tight-binding modeling of the chiral superlattice quantum geometry. a, Chiral superlattice band structure. **b**, Berry curvature k-space distribution of the low-energy superlattice band. **c**, Calculated Berry curvature dipole. **d**, Schematic of the chiral superlattice containing the $z+ix$ U1 and $z-ix$ U2 chiral displacements. **e**, Spatially-resolved Berry curvature at different x values in the superlattice, calculated by treating the slowly varying superlattice modulation as an adiabatic parameter and approximating each local region by a homogeneous tight-binding Hamiltonian $H(\mathbf{k};x)$. **f-j**, The same as panels (**a-e**) but for chiral superlattice plus the AFM order. Panel **h** shows the calculated AHE angle.



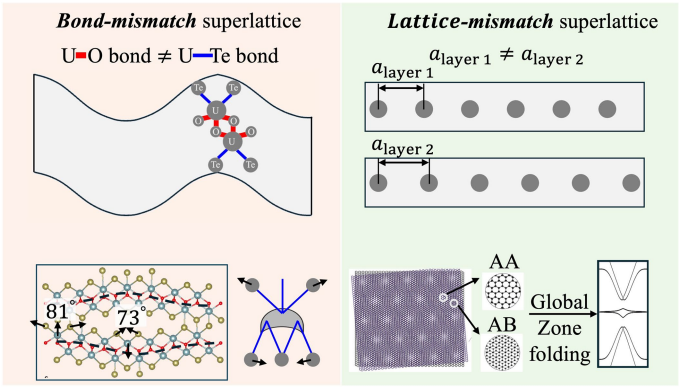
Extended Data Fig. 4 | Excluding weak ferromagnetism and the regular Hall effect as the main contribution of the AHE. a, Temperature dependence of in-plane and out-of-plane magnetic susceptibilities ($\chi_{//}$ and $\chi_{\perp}$). **b**, AHE and magnetization (measured by magnetic circular dichroism). The magnetic circular dichroism is the antisymmetric part of the optical circular dichroism, which naturally excludes the chiral circular dichroism (see details in SI.III.3). The net magnetization under finite magnetic field is given by $M = M_s + \chi_{\perp} B$. M_s is the spontaneous magnetization which was measured by the NV center magnetometry to be ~ 10 mμ_B per U ion. Due to the small M_s and large coercive field, large AHE is observed at zero magnetization, therefore demonstrating that the small net magnetization is a side product of the symmetry breaking. **c**, AHE as a function of the magnetization using the data in panel (**b**) for 129 K. **d**, We can further discern the different contributions to the Hall effect including the regular Hall effect, the weak ferromagnetism and the intrinsic AFM, i.e., $R_{AHE} = R_0 B + R_s M_s + R_{AFM}$. R_0 and R_s are slopes of the AHE vs. B field and AHE vs. magnetization curves. The different contributions at 129 K are shown here. The intrinsic AFM contribution strongly dominates.



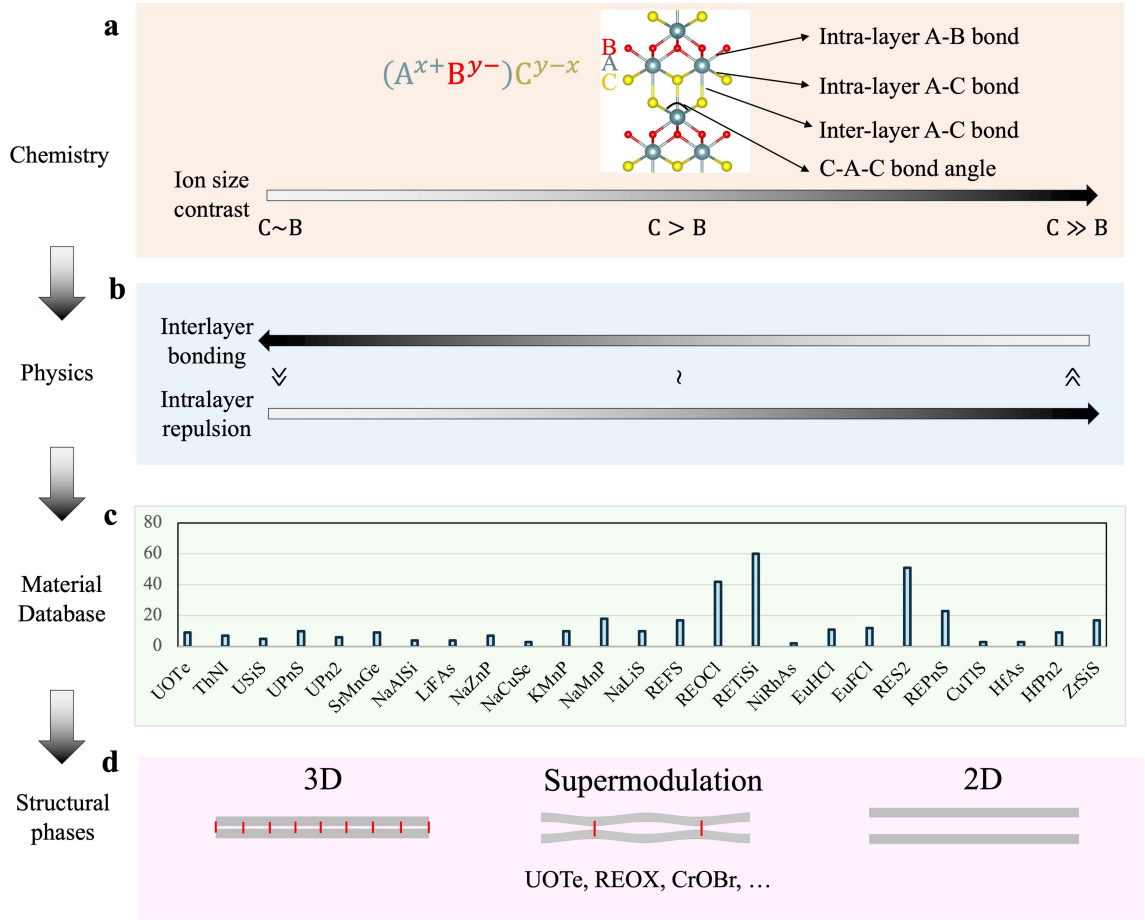
Extended Data Fig. 5 | Superlattice formation mechanism 1 - A comparison between UOS and UOTe. These two compounds are isostructural, but UOS has no supermodulation. A comparison of the nominal crystal structure shows that UOS has an additional interlayer bond connecting the U with the S in the next layer. This is enabled by the large S-U-S angle (82°), which resembles opening arms. Such an interlayer bond lowers energy. Forming similar interlayer bonding in UOTe is too energetically costly as the much longer U-Te bond length would laterally stretch the U-O-U central block at a similarly large bond angle. As a result, in the nominal unit cell of UOTe, the Te-U-Te bond angle is much smaller (77°), protecting the U-O-U central block from being stretched but in turn hindering the interlayer bonding.



Extended Data Fig. 6 | Superlattice formation mechanism 2 - Supermodulation as an intermediate phase. a, To form the interlayer bonding while keeping the central block unstretched, the layers decide to locally curve up/down with opposite signs in adjacent layers, which is the supermodulation. In this way, at specific locations, the Te-U-Te angle opens up (81°), allowing the interlayer bonding. At some other locations, the Te-U-Te angle decreases (73°), leading to an intralayer repulsion. The competition between the interlayer bonding and intralayer repulsion gives rise to the supermodulation in UOTe. **b**, More generally, we can consider three distinct phases: (1) 3D covalent, (2) 2D vdW, (3) supermodulation as an intermediate phase. The phase diagram is described by a Ginzburg-Landau theory (see main text). **c**, DFT-calculated phonon dispersions of UOS, UOTe and UOTe with artificially increased vdW gap.



Extended Data Fig. 7 | Bond-mismatch superlattice and lattice-mismatch superlattice. UOTe is a bond-mismatch superlattice, in which the superlattice strongly modifies the local U-O and U-Te bonding environment itself. This provides a real-space handle on the orbital composition and hopping amplitudes, which in turn produces spatially modulated Berry curvature, Berry-curvature dipole, and related quantum-geometric responses (see SI.II.5).



Extended Data Fig. 8 | Proposed design principle for chiral supermodulation. Based on the above mechanism and phenomenological theory, we propose a design principle that goes from chemistry to physics to materials. **a**, From chemistry, we can tune the size of the ions and the strength of chemical bonds. **b**, To physics, the above chemical tuning of ion size and bond strength effectively controls the interlayer bonding and intralayer repulsion energies. **c**, To materials, there are around 500 compounds isostructural to UOTe in the ICSD database. We have developed an empirical rule based on material parameters such as the ion size, the C-A-C bond angle, and the ratios of bond lengths including $r_1 = \frac{\text{Interlayer A − C bond length}}{\text{Intralayer A − C bond length}}$ and $r_2 = \frac{\text{Intralayer A − C bond length}}{\text{Intralayer A − B bond length}}$. **d**, Based on empirical rules, we can sift through the material database to identify the most promising materials (see SI.II.4).

Extended Data Table 1 | TEM displacement fitting values at 300 K

Layer	A_z^{U1} (pm)	A_x^{U1} (pm)	B_x^{U1} (pm)	ϕ_q^{U1} (deg)	ϕ_{2q}^{U1} (deg)	A_z^{U2} (pm)	A_x^{U2} (pm)	B_x^{U2} (pm)	ϕ_q^{U2} (deg)	ϕ_{2q}^{U2} (deg)	Ψ (pm)
Layer 1	31.7 ± 0.7	7.8 ± 0.7	1.5 ± 0.8	3.5 ± 5.6	-23.4 ± 27.8	31.5 ± 1.1	6.2 ± 1.1	0.9 ± 1.1	-1.0 ± 10.1	-22.1 ± 69.2	2.0
Layer 2	33.7 ± 0.6	7.9 ± 0.6	1.6 ± 0.6	6.4 ± 4.7	-27.5 ± 22.3	34.0 ± 1.0	7.0 ± 0.9	1.3 ± 1.0	-9.4 ± 7.9	-37.3 ± 42.6	3.1
Layer 3	32.8 ± 0.6	7.7 ± 0.6	1.6 ± 0.6	14.4 ± 4.9	-27.6 ± 23.8	34.8 ± 0.8	7.4 ± 0.8	2.1 ± 0.8	-12.9 ± 6.3	-23.6 ± 21.6	2.1
Layer 4	32.8 ± 0.7	7.4 ± 0.7	1.6 ± 0.7	10.2 ± 5.3	-5.3 ± 23.9	32.4 ± 1.1	8.2 ± 1.1	2.2 ± 1.1	-8.3 ± 7.9	-30.8 ± 28.2	3.1
Layer 5	32.6 ± 0.6	7.2 ± 0.6	1.7 ± 0.6	5.1 ± 5.1	-27.5 ± 21.0	32.6 ± 0.9	8.5 ± 0.9	2.5 ± 0.9	-18.8 ± 6.5	-32.5 ± 21.5	2.9
Layer 6	32.0 ± 0.6	7.6 ± 0.6	1.8 ± 0.6	-1.4 ± 5.0	-32.1 ± 20.5	33.7 ± 1.0	8.2 ± 1.0	2.8 ± 1.0	-0.5 ± 7.4	-37.5 ± 21.5	-3.2
Layer 7	33.7 ± 0.8	7.6 ± 0.8	2.3 ± 0.8	-1.7 ± 6.5	-54.9 ± 20.9	32.1 ± 1.0	7.7 ± 1.0	1.9 ± 0.9	6.8 ± 7.3	-15.5 ± 29.9	-3.8
Layer 8	36.1 ± 0.9	8.3 ± 0.9	1.5 ± 0.9	-1.5 ± 6.3	-29.5 ± 34.0	34.2 ± 0.8	7.5 ± 0.8	2.0 ± 0.8	-3.0 ± 6.6	-27.2 ± 24.4	-3.7
Layer 9	36.0 ± 1.0	9.2 ± 0.9	2.2 ± 1.0	4.2 ± 6.2	-45.2 ± 25.0	36.7 ± 1.2	8.5 ± 1.2	2.1 ± 1.2	-6.2 ± 8.1	-19.0 ± 32.4	-2.9
Layer 10	34.3 ± 0.8	8.4 ± 0.8	2.0 ± 0.8	8.0 ± 5.8	-27.8 ± 24.0	33.6 ± 1.2	7.9 ± 1.2	2.5 ± 1.2	-14.0 ± 9.1	-30.6 ± 28.1	-1.3
Layer 11	34.9 ± 0.7	8.6 ± 0.7	1.8 ± 0.7	13.9 ± 4.9	-19.5 ± 22.1	36.6 ± 1.1	8.5 ± 1.1	2.9 ± 1.1	-16.4 ± 7.5	-34.8 ± 22.1	3.2
Layer 12	33.6 ± 0.8	7.8 ± 0.8	2.3 ± 0.8	8.4 ± 5.8	-4.7 ± 19.2	33.5 ± 1.1	8.6 ± 1.1	2.1 ± 1.1	-10.0 ± 7.6	-48.0 ± 30.4	4.8
Layer 13	34.4 ± 0.9	8.0 ± 0.8	2.1 ± 0.9	6.8 ± 6.4	-22.1 ± 23.8	38.4 ± 1.4	8.4 ± 1.4	2.1 ± 1.4	-7.6 ± 10.0	-33.8 ± 39.0	3.7
Layer 14	32.2 ± 0.8	8.4 ± 0.7	1.3 ± 0.8	9.6 ± 5.3	-8.1 ± 32.7	33.1 ± 1.1	8.8 ± 1.1	2.1 ± 1.1	-1.0 ± 7.6	-10.6 ± 30.6	-3.1
Layer 15	31.4 ± 1.0	8.1 ± 1.0	2.3 ± 1.0	6.0 ± 7.6	-7.9 ± 26.7	31.0 ± 1.2	8.2 ± 1.2	2.4 ± 1.2	-5.0 ± 8.7	30.9 ± 28.6	0.4

Fitted displacement amplitudes, phases and net chirality (Ψ) for UOTe at room temperature.

Extended Data Table 2 | TEM displacement fitting values at 100 K

Layer	A_z^{U1} (pm)	A_x^{U1} (pm)	B_x^{U1} (pm)	ϕ_q^{U1} (deg)	ϕ_{2q}^{U1} (deg)	A_z^{U2} (pm)	A_x^{U2} (pm)	B_x^{U2} (pm)	ϕ_q^{U2} (deg)	ϕ_{2q}^{U2} (deg)	Ψ (pm)
Layer 1	32.2 ± 1.2	5.1 ± 1.1	1.9 ± 1.2	29.1 ± 13.4	-24.2 ± 34.3	31.3 ± 0.9	10.0 ± 0.9	0.2 ± 0.9	-4.4 ± 5.2	35.4 ± 292.0	5.7
Layer 2	32.1 ± 1.3	5.7 ± 1.2	2.9 ± 1.2	16.7 ± 12.7	-2.7 ± 24.9	31.9 ± 1.0	9.3 ± 1.0	2.1 ± 1.0	-0.5 ± 6.6	-34.3 ± 28.2	6.1
Layer 3	34.0 ± 1.3	5.4 ± 1.2	2.5 ± 1.2	18.3 ± 13.4	-21.9 ± 28.8	32.6 ± 1.1	9.3 ± 1.1	2.2 ± 1.1	4.3 ± 6.9	-15.3 ± 28.5	5.3
Layer 4	34.2 ± 0.8	7.2 ± 0.8	2.7 ± 0.8	20.4 ± 6.6	2.7 ± 17.7	34.1 ± 0.9	8.0 ± 0.9	1.6 ± 0.9	-0.3 ± 6.5	-69.3 ± 31.1	5.9
Layer 5	34.7 ± 1.3	7.6 ± 1.3	2.2 ± 1.3	15.0 ± 10.0	-18.1 ± 33.2	34.6 ± 1.2	9.4 ± 1.2	1.9 ± 1.2	-3.8 ± 7.6	-28.2 ± 35.8	5.2
Layer 6	34.3 ± 1.2	5.7 ± 1.2	3.1 ± 1.1	14.9 ± 12.1	-13.5 ± 22.5	33.2 ± 1.0	9.4 ± 0.9	1.4 ± 1.0	-4.9 ± 6.0	-39.0 ± 38.3	6.4
Layer 7	33.7 ± 1.2	6.9 ± 1.2	1.3 ± 1.2	9.0 ± 10.3	-38.5 ± 54.3	33.3 ± 1.1	10.2 ± 1.1	1.7 ± 1.1	-8.0 ± 6.5	-12.8 ± 37.4	3.8
Layer 8	32.7 ± 1.2	6.4 ± 1.2	1.2 ± 1.2	13.0 ± 11.2	-5.7 ± 59.3	30.7 ± 1.0	9.3 ± 1.0	1.1 ± 1.0	-4.9 ± 6.3	7.5 ± 49.1	3.9
Layer 9	31.3 ± 1.5	6.3 ± 1.5	2.5 ± 1.5	-2.0 ± 14.3	-30.9 ± 35.3	31.2 ± 0.9	9.3 ± 0.9	1.2 ± 0.9	4.9 ± 5.8	9.2 ± 42.3	5.0
Layer 10	34.6 ± 1.5	5.1 ± 1.4	2.1 ± 1.4	17.0 ± 16.5	7.7 ± 39.3	34.2 ± 1.3	9.6 ± 1.2	1.4 ± 1.2	-1.9 ± 7.8	41.0 ± 53.4	5.4
Layer 11	35.4 ± 1.5	7.2 ± 1.5	2.3 ± 1.5	11.3 ± 12.3	12.6 ± 38.1	34.8 ± 0.9	8.9 ± 0.9	1.1 ± 0.9	1.3 ± 6.0	-6.9 ± 47.9	5.1
Layer 12	37.0 ± 1.6	6.1 ± 1.5	3.1 ± 1.5	5.4 ± 15.0	16.0 ± 29.2	33.7 ± 1.0	10.5 ± 0.9	1.9 ± 0.9	-5.4 ± 5.4	14.7 ± 28.9	6.2
Layer 13	37.1 ± 1.5	7.8 ± 1.5	2.4 ± 1.5	1.6 ± 11.4	-25.4 ± 36.1	33.9 ± 1.0	10.2 ± 1.0	1.0 ± 1.0	4.1 ± 5.9	30.9 ± 56.3	5.4
Layer 14	34.6 ± 1.7	5.1 ± 1.7	2.3 ± 1.7	-0.7 ± 19.3	-23.5 ± 43.0	35.5 ± 1.3	10.3 ± 1.3	1.9 ± 1.3	-4.3 ± 7.5	-16.9 ± 39.0	5.7
Layer 15	32.6 ± 1.8	5.8 ± 1.7	2.7 ± 1.8	8.7 ± 17.8	-10.4 ± 37.8	34.3 ± 0.7	9.4 ± 0.7	0.4 ± 0.7	-1.2 ± 4.3	63.1 ± 97.8	6.1

Fitted displacement amplitudes, phases and net chirality (Ψ) for UOTe at 100 K.